

Volatile Organic Compound Detection Using Insect Odorant-Receptor Functionalised Field-Effect Transistors

by

Eddyn Oswald Perkins Treacher

A thesis submitted in fulfilment of the
requirements of the degree of
Doctor of Philosophy in Physics
School of Physical and Chemical Sciences
Te Herenga Waka - Victoria University of Wellington

Mar 2024



Table of contents

Acknowledgements	1
1. Vapour Sensing System for Transistor Biosensing	3
1.1. General Remarks	3
1.2. Technical Notes	4
1.2.1. Delivery System	4
1.2.2. Reference Sensors	5
1.2.3. Control System	8
1.3. Design	11
1.3.1. Initial Design	11
1.3.2. Stage I Design	13
1.3.3. Stage II Design	14
1.4. Calibration and Measurements of Vapour Flow	15
1.4.1. Chamber Flow Calibration	15
1.4.2. Sensor Responses to Vapour Flow	18
1.5. Summary	23
2. Characteristics of Pristine Carbon Nanotube & Graphene Field Effect Transistors	25
2.1. Introduction	25
2.2. Carbon Nanotube Network Morphology and Composition	26
2.2.1. Atomic Force Microscopy	26
2.2.2. Raman Spectroscopy	32
2.3. Electrical Characteristics of Pristine Devices	34
2.3.1. Python Analysis	34
2.3.2. Carbon Nanotube Network Devices	36
2.3.3. Graphene Devices	41
2.4. Aqueous Sensing of Phosphate Buffered Saline Concentration	43
2.4.1. Control Series and Baseline Drift	43
2.4.2. Sensing Series	47
2.5. Vapour Sensing with Ethyl Hexanoate	52
2.5.1. Baseline Drift	52
2.5.2. Sensing Series	52
2.6. Conclusion	52

Table of contents

Appendices	55
A. Vapour System Hardware	55
B. Python Code for Data Analysis	57
B.1. Code Repository	57
B.2. Atomic Force Microscope Histogram Analysis	57
B.3. Raman Spectroscopy Analysis	57
B.4. Field-Effect Transistor Analysis	57

Acknowledgements

69450

Rifat, Alex - vapour sensor
Erica Cassie - FET sensing setup
Rob Keyzers and Jennie Ramirez-Garcia - NMR spectra
Patricia Hunt - Computational chemistry

1. Vapour Sensing System for Transistor Biosensing

1.1. General Remarks

Through the adaptation of an existing setup, a custom vapour delivery system was developed to measure the response of field-effect biosensors to vapour. To achieve this goal, the new system needed to meet three requirements:

- The ability to automatically deliver a vapour to an enclosed environment in a controlled manner.
- The ability to collect measurements from a sensor device within that environment.
- The ability to collect data from off-the-shelf reference sensors monitoring the same environment, for comparison with data collected by the novel biosensor.

The existing system had a limited ability to meet the first two requirements, but was not able to take reference measurements of vapour flow. To implement new elements that would enable the system to fulfill all three requirements, a two-step development approach was taken across the course of the thesis. The changes made with each step of the redesign are outlined in Section 1.3.

Three mass flow controllers (MFC) were used to precisely control and monitor the flow of nitrogen into the system in units of standard cubic centimeters per minute (sccm). The manner in which these controllers were configured in the system is discussed in Section 1.2.1. The reference sensors chosen were a photoionisation detector (Ametek Mocon) and relative humidity and temperature indicator (Telaire). The photoionisation detector is able to monitor a wide range of volatile organic compounds, but cannot monitor compounds with an ionisation energy exceeding 10.6 eV. This includes nitrogen, oxygen, carbon dioxide, argon and water [1], [2]. Therefore, the photoionisation detector (PID) should not respond to either ambient air or standard nitrogen flow through the detector. As we would also like to monitor the presence of water vapour in the system, we use a relative humidity indicator (RHI). The operation of these reference sensors is discussed further in Section 1.2.2.

1. Vapour Sensing System for Transistor Biosensing

1.2. Technical Notes

1.2.1. Delivery System

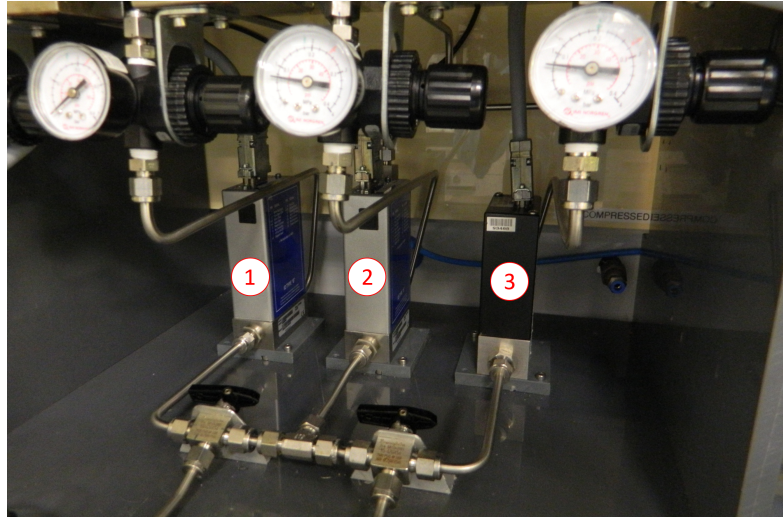


Figure 1.1.: Image of the three mass flow controllers (MFCs) of the Te Herenga Waka - Victoria University of Wellington cleanroom vapour delivery system, each with a regulator to set the pressure at the MFC inlet. (1) is the 20 sccm full-scale flow MFC, (2) is the 200 sccm full-scale flow MFC, and (3) is the 500 sccm full-scale flow MFC.

Three mass flow controller and their associated regulators sit in an covered enclosure, seen from the front in Figure 1.1. These are used to control the nitrogen flow rate through two different lines towards the chamber, the carrier line and dilution line. The lines merge at a mixing point about a metre before the device chamber, which contains the device being analysed. Each line consist of a mix of stainless steel and flexible PVC tubing, with various Swagelok fittings and valves. These valves include check valves, to ensure there is no backflow of vapour within the system. The carrier line connects flow to a 10 mL Schott bottle (Duran) containing analyte, shown in Figure 1.2. The vapour from the volatile analyte is then carried by nitrogen flow through the carrier line. A three-way valve determines whether the analyte vapour is then carried towards the mixing point or sent into the fumehood via the exhaust. The dilution line separately delivers flow to the mixing point, modifying the flow pushing the analyte vapour towards the chamber.

The setup is designed so that only one mass flow controller is directed through a single line at a time. The mass flow controller with a full-scale flow of 500 sccm (standard cubic centimeters per minute) can only be directed through the dilution line, and the mass flow controller with a full-scale flow of 20 sccm can only be directed through the carrier line. The mass flow controller with a full-scale flow of 200 sccm can be directed

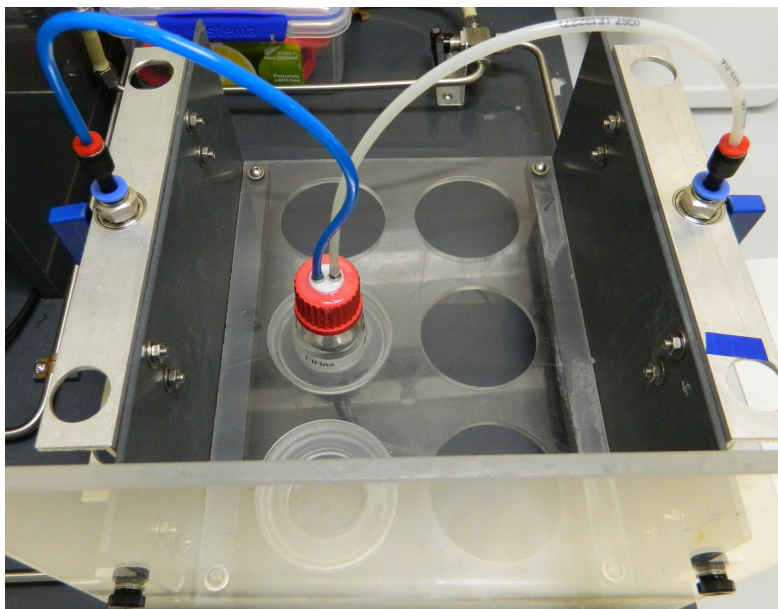


Figure 1.2.: Image of the analyte bottle, used to hold a volatile compound which provides vapour to the carrier line, either through bubbling or headspace sampling.

through the dilution line or carrier line. The electronic integration and programming of the mass flow controllers is described in Section 1.2.3.

1.2.2. Reference Sensors

Two reference sensors were added to the vapour delivery setup to compare the response to vapour by the fabricated sensor device with some reference signal. These reference sensors are a photoionisation detector (Ametek Mocon) and a relative humidity and temperature indicator (Telaire). The layout of these reference sensors (and their associated peripherals) relative to the device chamber is shown in Figure 1.3. These components are on a raised platform directly above the mass flow controller enclosure. Vapour flowing through the device chamber passes into a cylindrical manifold with three outlets. One outlet is the system exhaust, one flows into relative humidity indicator chamber, and one flows into the photoionisation detector. A dial-controlled micro diaphragm pump is used to set the flow rate from the manifold into the photoionisation detector, with a flowmeter used to monitor this flow rate.

The electronic integration and programming of the relative humidity and temperature indicator is described in Section 1.2.3. The photoionisation detector was connected to a laptop directly via USB, then controlled and monitored using the supplier-provided VOC-TRAQ II software package.

1. Vapour Sensing System for Transistor Biosensing

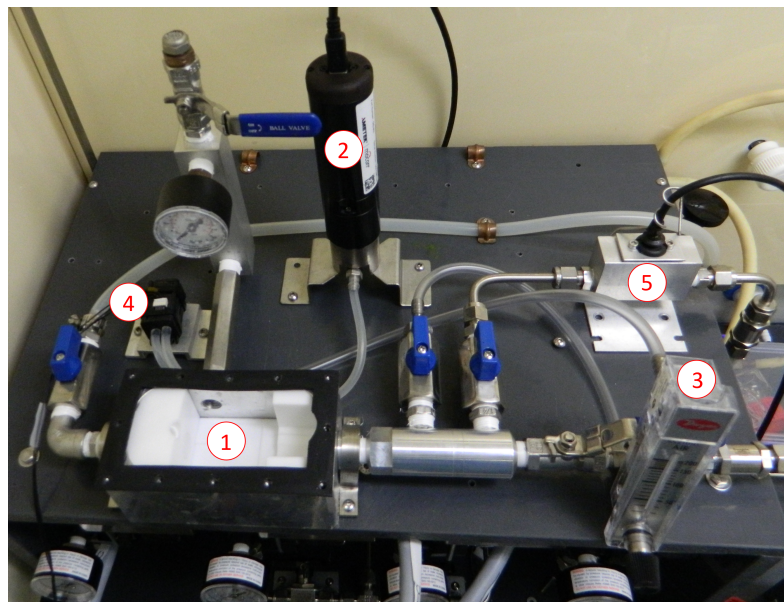


Figure 1.3.: Image of the device chamber, reference sensors and other related components. The components are labelled as follows: (1) Device chamber, (2) Photoionisation detector (PID), (3) Flowmeter from chamber to PID, (4) Micropump from chamber to PID, (5) Relative humidity and temperature monitor.

Relative Humidity and Temperature Indicator

The relative humidity and temperature indicator used here is a capacitive humidity sensor [3]. It consists of a capacitor with a hygroscopic polymer as the capacitor dielectric. As room temperature water has a much larger dielectric constant than the polymer dielectric, absorption of water by the polymer leads to increased sensor capacitance [4]. The sensor capacitance, corresponding to the amount of moisture absorbed by the polymer and therefore the relative humidity, is then translated by the sensor into a calibrated electronic output. This output is then processed using the hardware and software described in Section 1.2.3 to give a value for the relative humidity. The sensor has a quoted relative humidity (RH) accuracy of $\pm 2.0\%$ when RH is below 80%, and has a quoted temperature accuracy of 0.5°C [3].

The absolute humidity (AH), the mass of water vapour within a set volume, can be calculated in gm^{-3} using Equation 1.1, where $C = 2.16679 \text{ gKJ}^{-1}$, P_W is the water vapour pressure (in Pa) and T is the temperature (in K) [5].

$$AH = C \frac{P_W}{T} \quad (1.1)$$

For temperatures between -20°C and 50°C , water vapour pressure P_W (in hPa) can be approximated using Equation 1.2, where RH is relative humidity, T is temperature in $^\circ\text{C}$, A = 6.116441 hPa, m = 7.591386 and $T_n = 240.7263^\circ\text{C}$ [5].

$$P_W = RH \times A \times 10^{(mT/(T+T_n))} \quad (1.2)$$

Photoionisation Detector

A photoionisation detector (PID) can be used to continuously monitor volatile organic compounds by measuring the extent to which vapour molecules passing through the detector can be ionised. A small percentage of vapour molecules flowing into the detector diffuse into a sensor cavity. This cavity is bounded on each side by a pair of electrodes. A lamp in the body of the detector radiates UV light through a window into this cavity. The vapour molecules have their outer-most electrons excited and removed when struck with these high-energy photons. The ionised molecules then drift towards the sensor cathode, while free electrons drift towards the sensor anode. This results in a current proportional to the concentration of vapour molecules in the chamber. The current can then be amplified for a signal readout. To be detected, the ionisation energy of the molecules being monitored cannot exceed the energy of the incident UV light. Therefore, molecules of clean air will not be detected. Likewise, volatile organic compounds with high ionisation energy – such as methane – will not be recognised by the PID. Conversely, if the energy is required to ionise a volatile of interest is relatively low, the PID will generally show a relatively large response to that volatile [1], [2].

1. Vapour Sensing System for Transistor Biosensing

The photoionisation detector used in this work had a lamp energy of 10.6 eV, with a quoted response time of less than 2 seconds. Photoionisation detectors are designed to sensitively detect within a particular concentration range. PID sensors can become less sensitive after being exposed to very high concentrations of volatile gas. They can also become less sensitive if exposed to high levels of humidity or volatile substances known to contaminate the PID window, which are not used in this thesis. The typical sensitivity range of a PID can be stated in terms of the sensor response to isobutylene gas, which is typically used to calibrate PID sensors. The sensitivity of the the PID sensor used here was 10 ppb – 200 ppm. Calibration with a reference gas ensures the detector reads the true concentration of volatiles being detected, multiplied by some previously-documented factor called a “response factor”. However, these response factors can vary based on the design of the PID and various environmental factors [1], [2].

In this work, the PID was operated without end-user calibration. PID measurements were used to confirm the evolution of vapour presence in the chamber over time. It should be expected that sensor sensitivity will exhibit span drift over days or weeks, depending on changes in the local environment, and therefore measurements should not be treated as absolute measurements that correspond to a true concentration reading. A sampling rate of 1 s was used for all measurements. When sampling vapour concentration, baseline measurements of nitrogen flow through the PID were used as the zero concentration reference point.

The vapour of interest can be delivered to the PID either through diffusion or by means of a low-power pump. A micro diaphragm pump (Xavitech) was selected to pump the vapour from the chamber into the PID detector. A pump with a low maximum flow rate was selected since the PID requires a inlet flow of less than 300 sccm. As the pump is controlled using a unlabelled dial, a flowmeter was used to independently measure the flow rate through the micropump into the PID.

1.2.3. Control System

The vapour delivery system was controlled and monitored from a laptop connected to a National Instruments USB-6009 multifunction data acquisition input/ output module (DAQ). This USB-6009 DAQ connected to the mass flow controllers and relative humidity and temperature indicator (Telaire) via a custom-designed circuit board manufactured by PCBway. The outputs and inputs of the USB-6009 DAQ were set using custom LabView software. These electronic and software components of the vapour delivery control system are described in more detail below. The photoionisation detector (Ametek Mocon) was controlled from the same laptop with its own prepackaged software (VOC-TRAQ II).

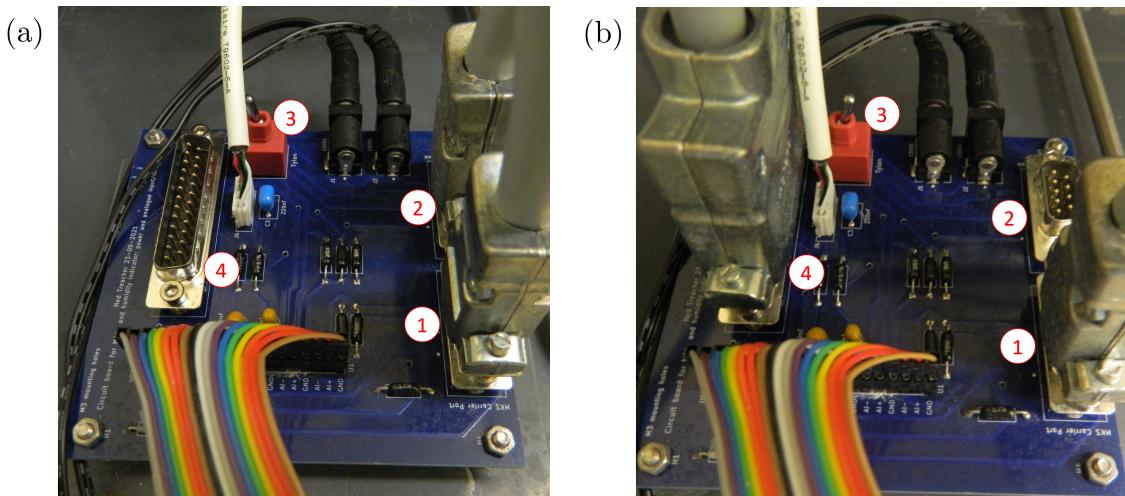


Figure 1.4.: Images of the vapour delivery control system circuit board, where (a) shows the low-flow configuration and (b) shows the high-flow configuration. Components are labelled as follows: (1) 9-pin carrier line port, (2) 9-pin dilution line port, (3) dilution port switch (determines which dilution line port is active), (4) 25-pin dilution line port. In (a), the 500 sccm full-scale MFC is connected at the 25-pin dilution line port, the 200 sccm full-scale MFC is connected at the 9-pin carrier line port and the red dilution port switch is towards “Tylan” (to the right). In (b), the 200 sccm full-scale MFC is connected at the 9-pin dilution line port, the 20 sccm full-scale MFC is connected at the 9-pin carrier line port and the red dilution port switch is towards “MKS” (to the left).

1. Vapour Sensing System for Transistor Biosensing

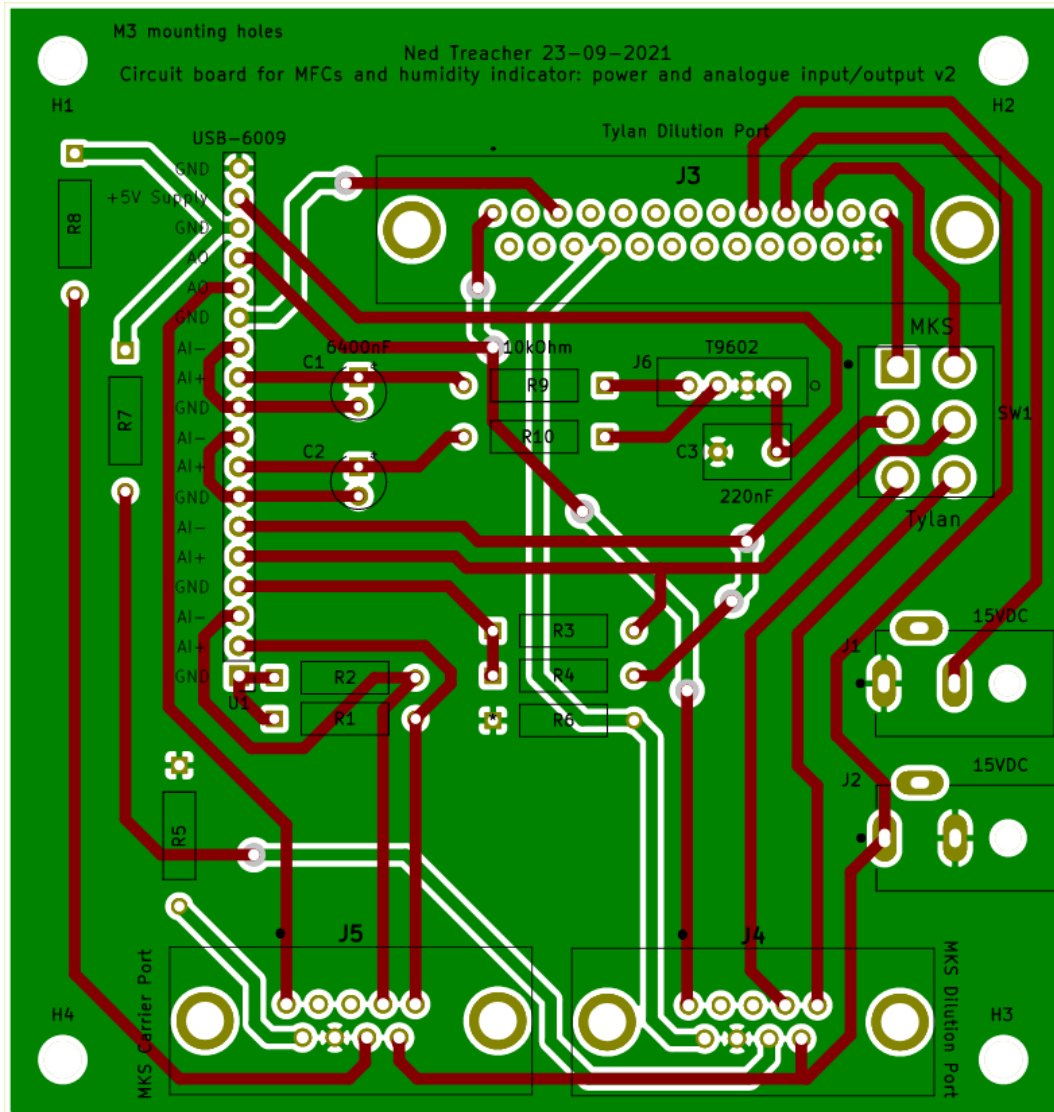


Figure 1.5.: Circuit board schematic for controlling and monitoring both the mass flow controllers and the relative humidity and temperature sensor. The relative humidity and temperature sensor is connected to the circuit board via the T9602 footprint. The mass flow controllers connect to the board in two configurations. The first (“high-flow”) configuration has the Tylan dilution and MKS carrier ports connected, with switch SW1 in the Tylan direction. The second (“low-flow”) configuration has both MKS ports connected, with switch SW1 connected in the MKS direction. Resistors R1-R6 are all 10 kOhm, while R7-R8 are both 0 Ohm. The circuit board was designed using the KiCad Layout Editor.

Electronics

The control circuit board used to connect the mass flow controllers and relative humidity and temperature indicator to the NI USB-6009 is shown in Figure 1.4. Only one mass flow controller can be set to provide flow to a specific line, and so only two mass flow controllers can be operational simultaneously during testing with the vapour delivery system. The control circuit board allows the user to set which two mass flow controllers are to be used during a specific test run. Figure 1.4 (a) shows the “high-flow” configuration, where the 500 sccm full-scale MFC is connected to the dilution line and the 200 sccm full-scale MFC is connected to the carrier line. Figure 1.4 (b) shows the “low-flow” configuration, where the 200 sccm full-scale MFC is connected to the dilution line and the 20 sccm full-scale MFC is connected to the carrier line. The design for the circuit board is shown in Figure 1.5, showing the pinout to the USB-6009 and the various components used to connect the MFCs, relative humidity indicator, and the power supply for the MFCs.

Software

Two LabView Virtual Instruments (VIs) were adapted from pre-existing VIs for operating the mass flow controllers and monitoring vapour flow into the device chamber, as well as monitoring temperature and humidity in the vapour delivery system’s manifold. These VIs were named “vapour-sensor-basic.vi” and “temp-and-humidity-basic.vi”. A third VI was developed in parallel which combined the first two Virtual Instruments and allowed the user to set a sequence of values for the output flow from the mass flow controllers before an experimental run. This VI was named “vapour-sensor-sequence-timestamped.vi”. Flow rate, relative humidity and temperature data were then saved as .lvm files. The LabView VIs described here are available on request.

1.3. Design

1.3.1. Initial Design

The initial design of the vapour delivery system, as shown in Figure 1.6, was relatively simple. No reference sensors were included in the setup, and only one channel could be characterised without opening the chamber and changing the position of the device. However, as constructed it worked well as a self-contained system, which was able to deliver vapour to a device channel while measuring current across the channel. The original system is shown in Figure 1.7, and the circuit board used to control it is shown in @fig-original-pcb. A 500 sccm full-range MFC (Tylan) was placed on the dilution line, and a 200 sccm full-range MFC (Tylan) was placed on the carrier line. A glass container for analyte was present on the carrier line, with a vapour trap upstream to collect any

1. Vapour Sensing System for Transistor Biosensing

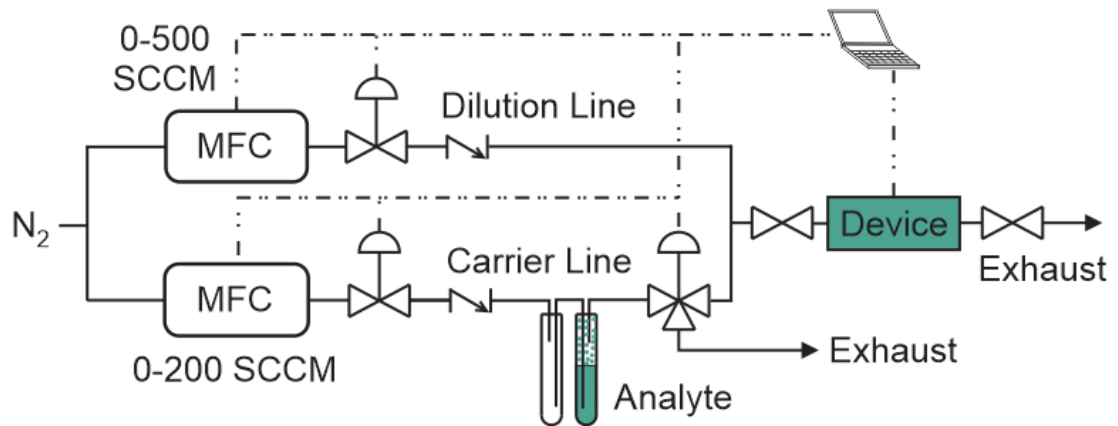


Figure 1.6.: P&ID of the original vapour delivery system

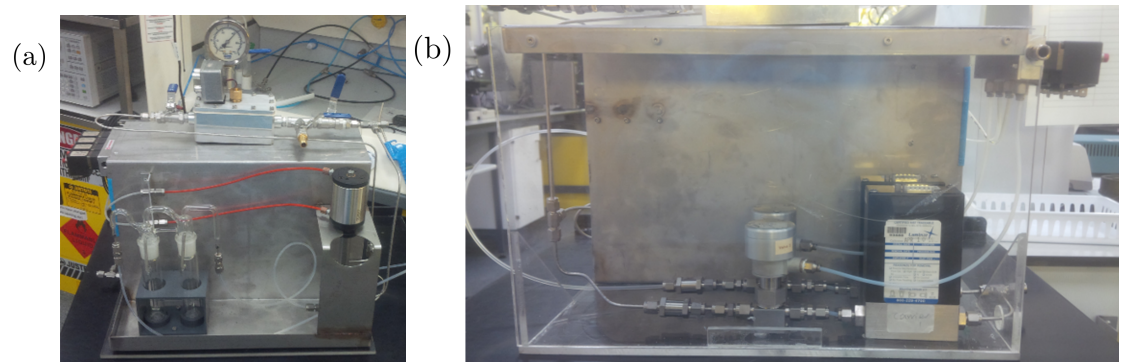


Figure 1.7.: The original vapour delivery system setup, where (a) shows the front of the system, including the device chamber, analyte bottles and four-way valve, and (b) shows the back of the system, including the mass flow controllers and solenoid valves.



Figure 1.8.: The control circuit board for the original vapour delivery system.

backflow. The vapour trap was removed in later iterations due to the presence of a check valve to prevent backflow. The device chamber and mass flow controllers were connected to a laptop and an Agilent 4156C semiconductor parameter analyser and controlled using LabView.

1.3.2. Stage I Design

The first stage of the vapour delivery system redesign, as shown in Figure 1.9, was implemented in Nov 2021. This system introduced the ability to use a 20 sccm full-range MFC (MKS Instruments) for carrier line flow and a 200 sccm full-range MFC (MKS Instruments) for either carrier or dilution line flow, to give better control when using low flow rates. The reference sensors were also implemented, with each sensor connected in parallel to the chamber exhaust. Through testing the system with ethanol and acetone as analytes, the following issues with this implementation of the setup were identified:

- With the system connected to the lab supply of nitrogen, pressure changes in the line due to nitrogen use elsewhere in the lab impacted the pressure at the MFCs and the flow through the lines.
- The pressure indicator used for the device chamber had a much wider range than the pressure reached before nitrogen began to leak out of the PVC tubing; this meant pressure changes in the chamber, resulting from closing the exit valves while nitrogen flow entered the chamber, did not register on the indicator.
- The PID responded unexpectedly slowly to changes in vapour concentration in the chamber. For example, after acetone or ethanol vapour had been run through

1. Vapour Sensing System for Transistor Biosensing

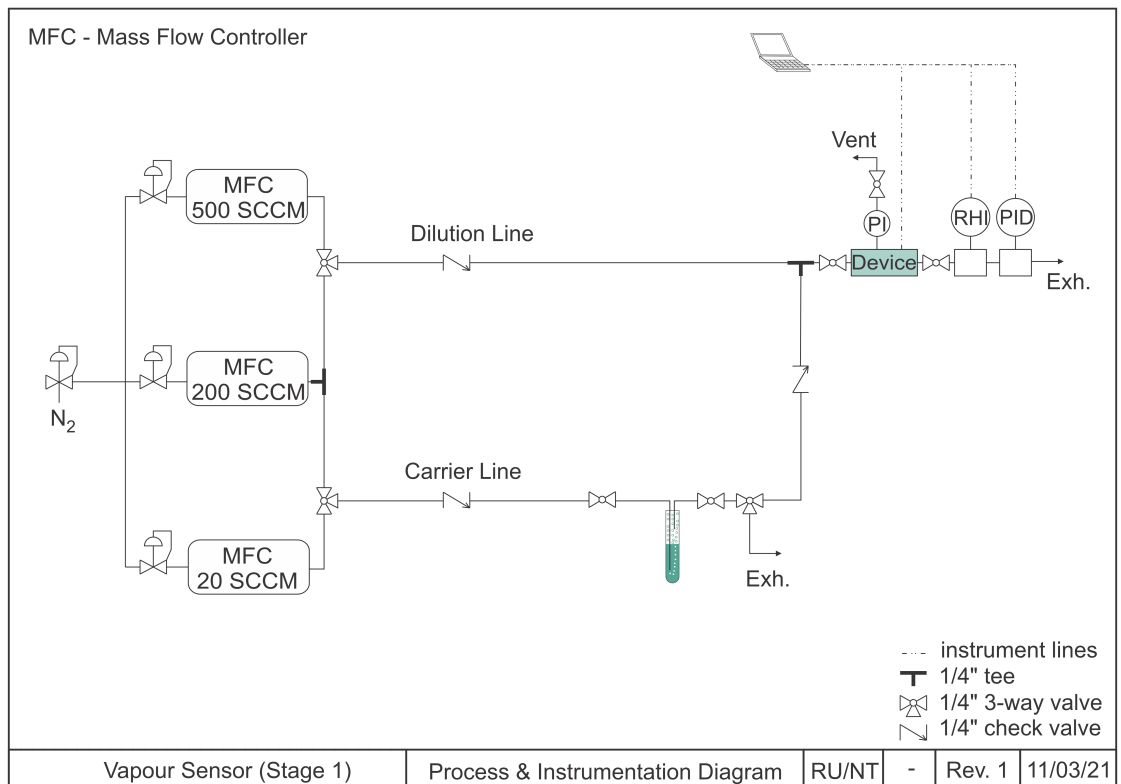


Figure 1.9.: P&ID of the Stage I vapour delivery system.

1.3. Design

the chamber, running clean nitrogen through the system for 3 hours was required before the PID returned to a constant baseline reading.

- There was no way to ensure the device chamber was free of analyte vapour before an experimental run aside from running nitrogen through the dilution line. After prolonged use, condensed analyte was sometimes visible in the PVC lines of the delivery system.

These issues, along with various minor structural and design issues, were addressed in the second-stage implementation of the system.

1.3.3. Stage II Design

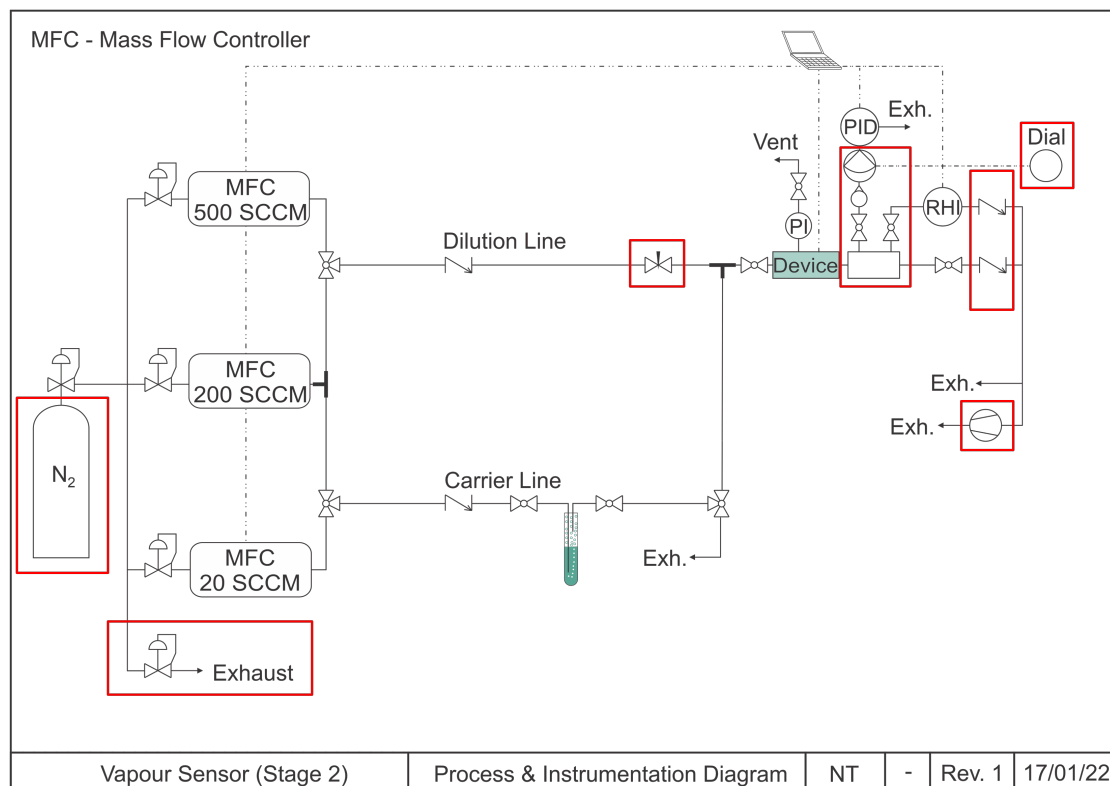


Figure 1.10.: Process & instrumentation diagram (P&ID) of the second-stage design for the vapour delivery system. Red outlines indicate additions introduced to the system subsequent to the first stage design.

Figure 1.10 gives an overview of the second-stage design for the vapour delivery system setup. This stage of the redesign was implemented between Jan and May 2022. Changes from the first stage included:

1. Vapour Sensing System for Transistor Biosensing

- The addition of a N₂ cylinder (152D size) as the source of nitrogen for the system to replace the lab supply.
- A pressure indicator with a lower pressure range was used, which could register pressure changes within the device chamber.
- A chamber manifold was placed before the exhaust with outlets into the PID and RHI.
- A micro diaphragm pump was introduced between the manifold and PID to supply the PID with vapour from the chamber, and a flowmeter was placed before the pump to measure the flow rate out of the chamber to the PID. The PID was then seen to respond quickly to system changes (discussed further in Section 1.4).
- A piece of PVC tubing was placed at the PID outlet to limit air from the fumehood entering the PID when the micropump was off.
- Valves were placed before all system components so that the device chamber and post-analyte bottle carrier line could be evacuated with a roughing pump without potentially affecting components.
- Check valves were placed at the exhaust to prevent backflow from the roughing pump into the delivery system.

These changes largely addressed the issues identified in Section 1.3.2.

1.4. Calibration and Measurements of Vapour Flow

1.4.1. Chamber Flow Calibration

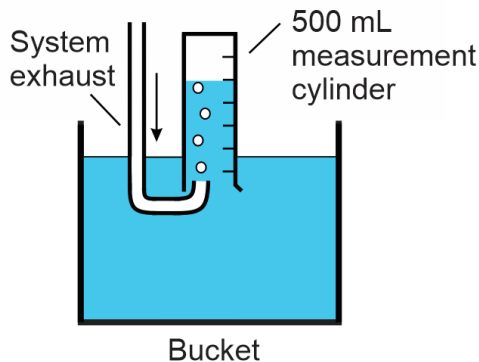


Figure 1.11.: Setup for calibration of mass flow controllers using the water displacement method.

1.4. Calibration and Measurements of Vapour Flow

A water displacement test was carried out to determine the relationship between the flow rate measured by the mass flow controllers and the actual flow rate passing through the chamber. All valves were set so that both the dilution and carrier lines followed a single path. Both these paths went through the device chamber and out through the system exhaust. An empty analyte bottle was placed on the carrier line. The system exhaust was placed into a bucket filled with tap water, with the outlet sitting beneath an upturned 500 mL measurement cylinder, as pictured in Figure 1.11. The cylinder was used to measure the volume of displaced water over time, which is equivalent to the rate of change of nitrogen volume entering the cylinder from the exhaust. As leaks in the manifold and exhaust line were not detected when leak testing with bubble solution, it can be safely assumed that the rate at which nitrogen exits the exhaust is equivalent to the nitrogen flow rate through the device chamber.

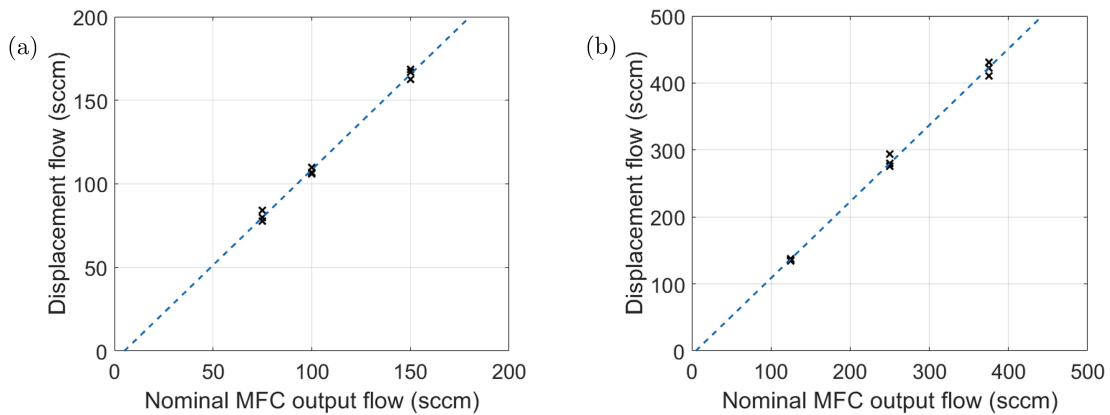


Figure 1.12.: Calibration curves for the 200 sccm full-scale MFC through the carrier line (a) and the 500 sccm full-scale MFC through the dilution line (b).

The time taken to displace a fixed volume of water was measured three times for a series of constant flow rates, both for the 200 sccm MFC (MKS) on the carrier line and the 500 sccm MFC (Tylan) on the dilution line. The displacement flow rate corresponding to each measurement could then be found by dividing volume by time. These measurements, of displacement flow relative to nominal flow through the MFC, are shown in Figure 1.12. The flow through the chamber was offset from the nominal flow reading from the mass flow controllers, with a strong linear relationship between the two measurements. A linear least-squares fit was performed, where coefficients a_1 and a_2 were found for the linear relationship $D = a_1d + a_2$, where d is nominal flow from the MFC and D is measured displacement flow. A 95% confidence interval for each fit was also obtained. For the 200 sccm MFC flow through the carrier line, values of $a_1 = 1.14 \pm 0.07$ and $a_2 = -6 \pm 8$ were obtained, while for the 500 sccm MFC flow through the dilution line, values of $a_1 = 1.14 \pm 0.06$ and $a_2 = -6 \pm 16$ were obtained.

It appears that the offset between the measured displacement flow and nominal output flow is not due to leaks in the system, since the offset indicates measured flow exceeds

1. Vapour Sensing System for Transistor Biosensing

the nominal flow. Instead, the offset appears to be a systematic error introduced by the electronics or software used to record the output flow from the MFCs. The identical offset between measured and nominal flow observed for each MFC, even when placed on different lines to the chamber, further strengthens the likelihood of the offset being due to the control side of the system. Furthermore, due to the identical offset for each of the carrier and dilution MFCs, the same offset should apply to a mixture of flows on each line. For example, a 200 sccm nominal flow through the dilution line from the 500 sccm full-scale MFC should have a roughly identical actual flow rate to a 50 sccm nominal flow through the dilution line and a 150 sccm flow through the carrier line. In this work, tests performed with the vapour delivery system have flow rate stated in terms of their nominal value, but the reader should keep in mind the $1.14\times$ offset from the actual chamber flow.

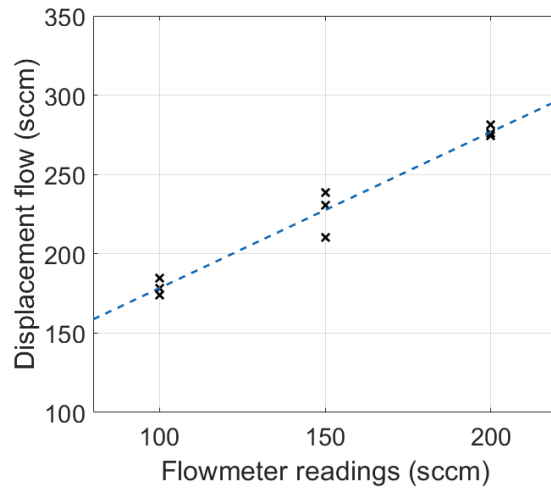


Figure 1.13.: Calibration curve for the PID flowmeter, comparing flowmeter readings with flow rate of water displacement.

The time taken to displace a fixed water volume was also measured three times for a series of constant flow rates through the flowmeter from the chamber to exhaust. A linear relationship was obtained between flowmeter readings and actual displacement, as shown in Figure 1.13. Expressing the relationship as $D = b_1 f + b_2$, where f is the flowmeter reading and D is measured displacement flow, values of $b_1 = 1.0 \pm 0.2$ and $b_2 = 80 \pm 25$ were obtained. A 200 sccm flow rate through the dilution line from the Tylan MFC, corresponding to a ~ 230 sccm actual flow rate through the chamber, would therefore be measured as a ~ 150 sccm flow rate by the flowmeter. Subsequent measurements showed that the linear relationship in Figure 1.13 breaks down for flowmeter readings $\lesssim 75$. For example, a 50 sccm flow on the flowmeter was found to correspond to 85 sccm of measured displacement flow. By disconnecting the flowmeter from the PID micropump and closing all valves out of the manifold except the valve exiting to the flowmeter (see Figure 1.10), the nominal flow on the MFC could be directly compared to the flowmeter reading. In this manner, the actual flow rate of readings $\lesssim 75$ sccm on

1.4. Calibration and Measurements of Vapour Flow

the flowmeter could be quickly obtained.

1.4.2. Sensor Responses to Vapour Flow

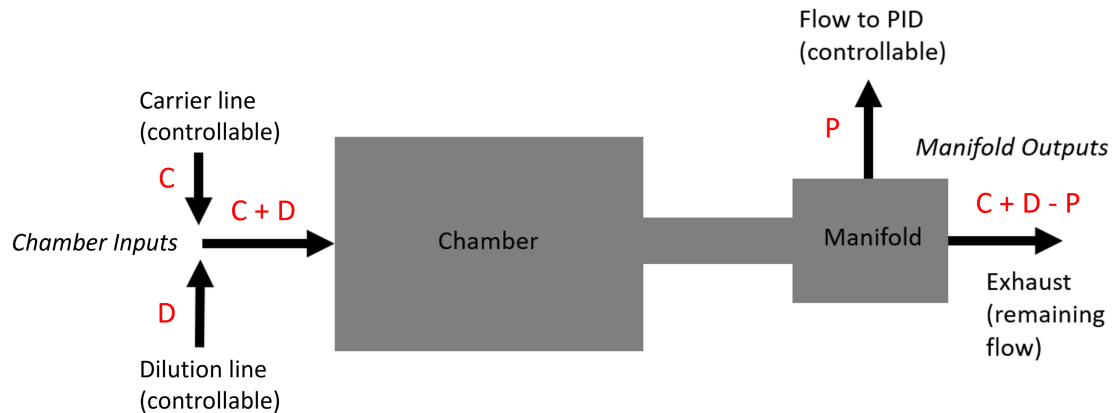


Figure 1.14.: Simplified schematic showing the flow into and out of the device chamber and manifold of the delivery system. The input flows from the carrier and dilution line are represented by C and D, and the output flow through the PID is represented by P. The exhaust can either flow past the relative humidity indicator or straight to the fumehood. This diagram assumes that flow through leaks in the chamber and manifold is low enough to be considered negligible, which was confirmed by leak testing with bubble solution.

Once the rate of flow through the device chamber had been calibrated, the next step was to verify the correct operation of the reference sensors used in the system. Various flow rates in and out of the chamber were used to calibrate and verify the reference sensors. These flows in and out of the chamber are labelled on the simplified schematic in Figure 1.14.

Relative Humidity Indicator

To test the relative humidity indicator (RHI), all valves out of the chamber were sealed except for the valve for the relative humidity indicator chamber. This meant all flow coming out of the system would pass through the relative humidity indicator chamber ($P = 0$ sccm and exhaust goes to RHI in Figure 1.14). Continuous nitrogen flow was then placed through the chamber until relative humidity dropped to about 20%. 10 mL of deionised water was placed into the analyte bottle. A series of different flow rates through each line was sent to the chamber, with the sequence of flow rates shown in Table 1.1 (t = time, C = carrier line flow rate, D = dilution line flow rate). Note that

1. Vapour Sensing System for Transistor Biosensing

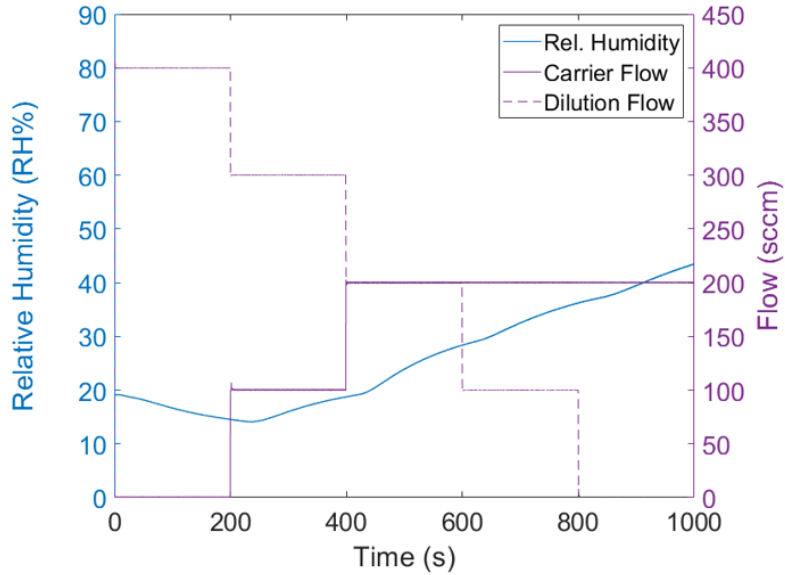


Figure 1.15.: Relative humidity readouts from the relative humidity indicator juxtaposed with flow rates from the dilution line and carrier lines of the vapour system, with 10 mL deionised water in the carrier line analyte bottle.

between 230 s and 630 s, the total flow rate remains the same, but the ratio of dilution to carrier flow differs.

Table 1.1.: Flow sequence for testing relative humidity indicator.

t (s)	C (sccm)	D (sccm)
200	0	400
200	100	300
200	200	200
200	200	100
200	200	0

Figure 1.15 shows flow purely from the dilution line decreases humidity as measured by the Telaire sensor, while flow from the analyte bottle containing deionised water increases humidity, as expected. It also shows that in regular 200 s intervals, an uptick in the increase of relative humidity occurs, which then begins to flatten out. Each gradient uptick occurs about 50 s after a corresponding increase in flow through the carrier line. It therefore appears that each interval corresponds to an increase of water vapour flow, where 50 s is the time taken for the increased concentration of water vapour to first reach the relative humidity indicator.

Over the full 800 s of carrier line flow, relative humidity increases from a minimum of $14.0 \pm 2.0\%$ to a maximum of $43.6 \pm 2.0\%$. The temperature in the chamber remained

1.4. Calibration and Measurements of Vapour Flow

between $21.0 \pm 0.5^\circ\text{C}$ and $22.0 \pm 0.5^\circ\text{C}$ over the entire measurement period. Combining equations Equation 1.1 and Equation 1.2 from Section 1.2.2, we find that the absolute humidity in the chamber reaches a low of $2.6 \pm 0.4 \text{ gm}^{-3}$ at 238.1 s, 38.1 s after the initial onset of carrier flow, and a high of $8.4 \pm 0.5 \text{ gm}^{-3}$ at 998.8 s, after 798.8 s of carrier flow through the chamber. The clear response of the Telaire RHI to water vapour flow through the carrier line confirms that this sensor is working as expected.

Photoionisation Detector

To test the photoionisation detector, the device chamber and carrier line were first purged of vapour through the exhaust using a roughing pump, with the PID valve closed to protect it from the pump. The PID valve was then opened, the micropump was set to 150 sccm as read by the flowmeter. During testing with the PID, the total flow into the chamber was set at 200 sccm as read by the Tylan mass flow controllers. The calibration curves in Section 1.4.1 show that the actual flow C + D was then therefore approximately the same as the actual flow rate into the PID, P. A flow of 200 sccm nitrogen was placed through the dilution line to the chamber for 10 minutes until successive concentration readings from the PID were either approximately constant, or until baseline drift was small enough to be considered negligible. These measurements were then used as the baseline (0 ppm) for subsequent measurements. 5 mL of the volatile organic compound ethyl hexanoate (EtHex) was placed into the analyte bottle. A flow of 150 sccm was then sent through the carrier line and 50 sccm through the dilution line for 600 s. The same procedure was performed on two separate dates spaced three days apart (23 Feb and 26 Feb) to check that the measured PID response to ethyl hexanoate vapour pumped out of the manifold was repeatable.

The responses from each date are shown in Figure 1.16. In Figure 1.16 (a), the response corresponding to each measurement date is shown unnormalised, with the parts per million concentration shown relative to the nitrogen baseline as recorded by the PID. Both measurements show little to no response to vapour for approximately 50 s, which seems to be the time taken for vapour to first reach the PID. Over the next 100s, there is a rapid increase in vapour concentration detected, which then settles to a constant concentration at about 300 s. This appears to be the maximum concentration of EtHex vapour that can be contained by the chamber in this configuration. There is approximately a 200 parts per billion difference in maximum concentration between the measurement on each date.

However, this is not unexpected. As discussed in Section 1.2.2, the PID is being run uncalibrated, and some drift of the sensitivity of the sensor due to environmental changes is highly likely. To check that the PID records the same evolution of vapour flow with time, regardless of its sensitivity, the measurements from both dates were then normalised with respect to the maximum concentration reading. Figure 1.16 (b) shows that once normalised, the rate of change in concentration with time is almost identical between the two measurement sets. This test verifies that the evolution of vapour

1. Vapour Sensing System for Transistor Biosensing

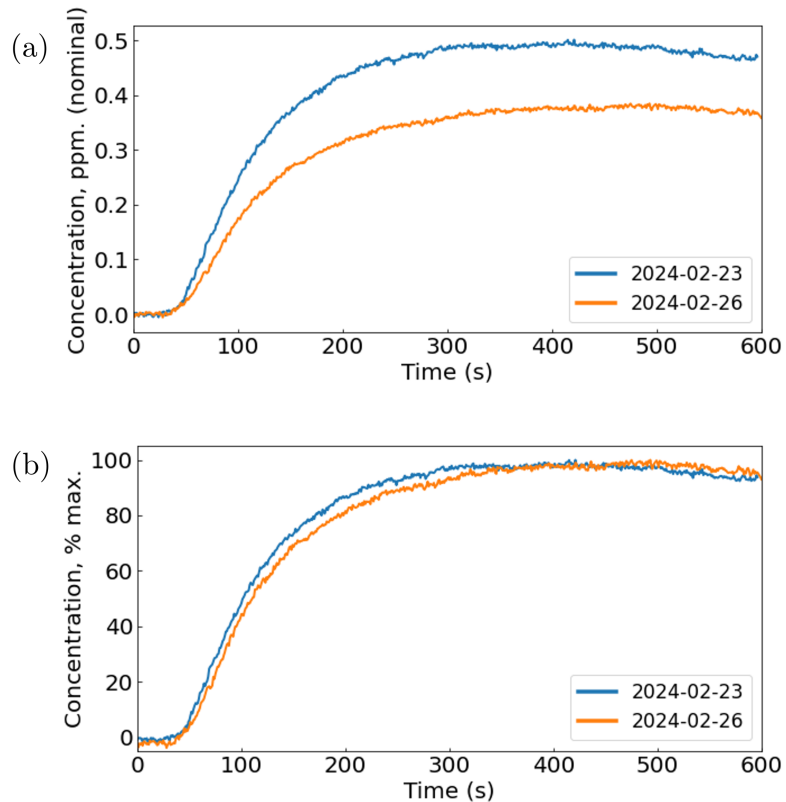


Figure 1.16.: The response of the photoionisation detector to ethyl hexanoate vapour over 600 s of exposure is shown relative to the 200 sccm nitrogen flow baseline in (a), and normalised with respect to the maximum reading in (b).

1.4. Calibration and Measurements of Vapour Flow

concentration of the device chamber can be repeatably measured using the PID in the vapour delivery system.

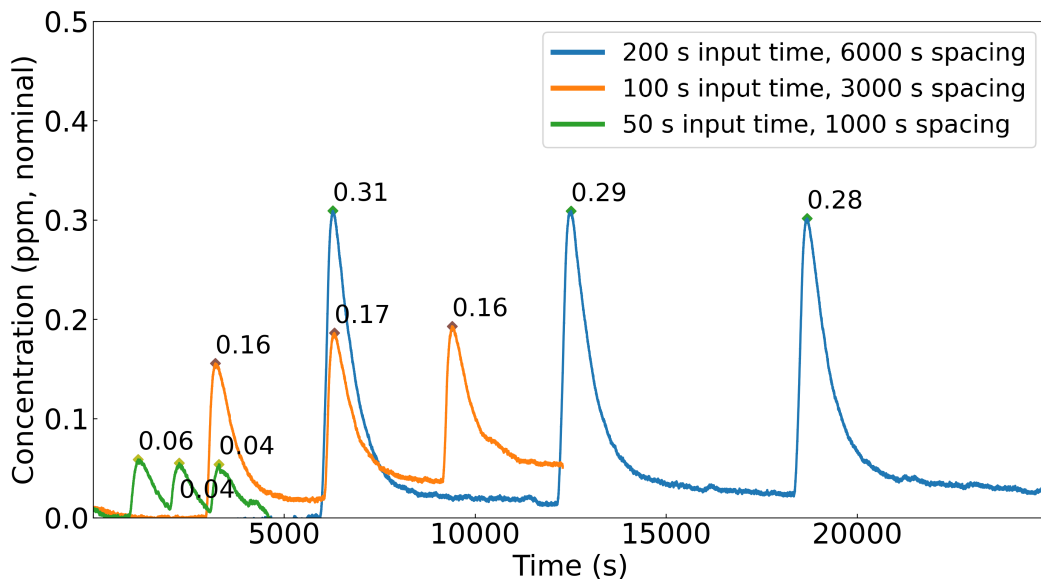


Figure 1.17.: The response of the photoionisation detector to 3 evenly-spaced intervals of ethyl hexanoate vapour entering the device chamber, relative to a 200 sccm nitrogen flow baseline. Input intervals were either either 50 s, 100 s or 200 s in length. During each input interval, 150 sccm carrier flow and 50 sccm dilution flow was placed through the chamber.

A further series of tests were performed to verify whether it was possible to compare different concentrations of vapour in the chamber using the PID. All testing was performed on the same day to minimise sensitivity drift. For each test, the system was purged of vapour and the total dilution flow into the chamber was set at 200 sccm as read by the Tylan mass flow controller. Flow out of the chamber to the PID was set at 100 sccm as read by the micropump flowmeter, and the almost-constant nitrogen baseline after 10 minutes was set as the PID zero point. 5 mL of the volatile organic compound ethyl hexanoate (EtHex) was placed into the analyte bottle. During each test, 200 sccm was continuously flowed through the dilution line, except during three evenly spaced intervals of equal length. During these intervals, 150 sccm flow was placed through the carrier line and 50 sccm flow placed through the dilution line. In each test, the input interval time was varied to examine its effect on maximum vapour concentration recorded by the PID. As it took longer for the PID to return to a constant baseline with increased input intervals, when the input interval was increased, the spacing between intervals was also increased.

The results of three tests, with input intervals of 50 s, 100 s and 200 s, are shown in Figure 1.17. Each interval of carrier flow corresponds to a rapid increase in concentration, which reaches a peak, then decreases. The maximum concentration reached for

1. Vapour Sensing System for Transistor Biosensing

each interval is shown above the corresponding peak. Note that the maximum concentration label does not correspond to the difference between the original baseline and the maximum concentration of each peak. Instead, it corresponds to the difference between the concentration measurement at a set time before the onset of carrier flow and the maximum concentration reached. For each test, this set time is 5% of the spacing time used, 50 s, 150 s and 300 s respectively. This approach was taken to account for what appears to be drift from the original 0 ppm baseline. This variable baseline drift was particularly significant for the 100 s interval measurements, where concentration measurements settled to a new baseline of ~ 0.05 ppm after the third peak.

The values of three concentration maxima in each test are highly consistent, with only a ± 0.02 ppm margin of error. This experiment demonstrates that if tests using the PID are performed during the same day, placing the same vapour flow into the PID for the same interval of time in each test, it is possible to measure the same maximum concentration with the PID. It furthermore indicates that the placing the same amount of vapour flow into the chamber for a set amount of time leads to a reproducible concentration of vapour building up within the chamber.

1.5. Summary

A custom vapour delivery system was made suitable for field-effect biosensor work through ensuring a range of flows could be delivered through the system and that reference sensors were available for corroboration with the readings on the field-effect biosensors. Two new mass flow controllers with different maximum flow rates and two reference sensors, a relative humidity and temperature sensor and photoionisation detector, were introduced to the system in a two-stage design process. A new electronic control system and LabView software were designed and constructed for the altered delivery system. The nitrogen flow through the system was then calibrated using water displacement testing, and it was verified that the reference sensors both worked as expected.

2. Characteristics of Pristine Carbon Nanotube & Graphene Field Effect Transistors

2.1. Introduction

A range of methods were followed to fabricate carbon nanotube network and graphene field-effect transistors for biosensor use. This chapter therefore looks to use the characterisation techniques outlined in the previous chapter to compare and contrast the device channel morphologies and electrical characteristics resulting from various methods.

The three carbon nanotube film types used for devices were the solvent-deposited, surfactant-deposited and steam-assisted surfactant-deposited (steam-deposited) films discussed in the previous chapter. As minor changes were made to fabrication processes throughout the thesis, the fabrication dates of devices used are stated, which can be cross-referenced with **?@sec-fabrication** to identify the specific process used. Atomic force microscopy and Raman spectroscopy was performed on the carbon nanotube networks to identify the distribution of carbon nanotube diameters and the defects present on the carbon nanotube networks. Electrical characterisation was then used to see how the morphology of each film type affects the performance of the completed devices. Both back-gated and liquid-gated transfer characteristics were compared, as well as key parameters taken from the liquid-gated characteristics. The electrical behaviour of liquid-gated graphene devices was also examined, as well as the impact of water on the performance of back-gated devices for vapour sensing use.

Finally, as a control measurement for liquid-gated sensing and to verify the behaviour of the pristine device as a sensor, a salt concentration sensing series was performed with a steam-deposited carbon nanotube network device. The device characteristics were taken and device drift was examined and modelled. The sensing series was performed by successively diluting 1XPBS electrolyte in the polydimethylsiloxane ‘well’ (electrolyte container) while passing a current through the device, and measuring the current response to dilutions. Various filters were applied to the collected data to better understand the signal change.

2.2. Carbon Nanotube Network Morphology and Composition

2.2.1. Atomic Force Microscopy

Figure 2.1 shows a side-by-side comparison of the surface morphology of carbon nanotube films fabricated using the methods described in ?@sec-dep-carbon-nanotubes. These images were collected using an atomic force microscope and processed in the manner described in ?@sec-afm-characterisation. Figure 2.1a shows a film of carbon nanotubes deposited in solvent, Figure 2.1c shows a film of carbon nanotubes dropcast in surfactant, and Figure 2.1e shows carbon nanotubes dropcast in surfactant in the presence of steam. As discussed in previous works using solvent-based deposition techniques for depositing carbon nanotubes, in each network multi-tube bundles form due to strong mutual attraction between nanotubes [6]–[9]. However, when surfactants are present, they adsorb onto the carbon nanotubes and form a highly repulsive structure able to overcome the strong attraction between nanotubes. This repulsion keeps the individual carbon nanotubes more isolated [10]–[14]. The diameter range provided by the supplier for the individual carbon nanotubes used is 1.2 – 1.7 nm, while the length range is 0.3 – 5.0 μm (Nanointegris).

It has previously been demonstrated that the diameter range of deposited single-walled carbon nanotubes can be modelled via a normal or Gaussian distribution [15]–[17]. However, when the height profiles from the $2.5 \mu\text{m} \times 2.5 \mu\text{m}$ AFM images are directly extracted and binned, as plotted in black in Figure 2.1, the histograms obtained do not follow a normal distribution. One reason for this result is the surface roughness of the silicon dioxide substrate. The carbon nanotubes do not lie perfectly level on a perfectly level silicon oxide substrate. In practice, both the SiO_2 substrate and the surface of the carbon nanotubes both have a degree of roughness. To find the contribution of surface roughness to the height profile histogram corresponding to each network deposition method, silicon dioxide substrates were modified using the same processes as in Figure 2.1 but without carbon nanotubes present in the solutions used. $2.5 \mu\text{m} \times 2.5 \mu\text{m}$ AFM images of the modified surfaces are shown in Figure 2.2.

In Figure 2.2, it appears that each substrate surface has a roughness that follows a normal distribution with some degree of skewness. Figure 2.2b and Figure 2.2d are negatively skewed distributions. The fitted skew-normal distribution in Figure 2.2b has a skew parameter α (or shape parameter) of -3.2, a location parameter ξ of 2.2 nm and a scale parameter ω of 0.5 nm, while in Figure 2.2d $\alpha = -2.2$, $\xi = 2.2$ nm and $\omega = 0.5$ nm. ξ and ω correspond to the mean and standard deviation of the skew-free normal distribution when α is set equal to zero [18]. The close correspondence between ξ and ω for these distributions but not α implies that the skewness is a variable imaging or processing artifact rather than a physical property of the surface. Without distortion, the roughness of a clean SiO_2 surface should follow a normal distribution [19].

2.2. Carbon Nanotube Network Morphology and Composition

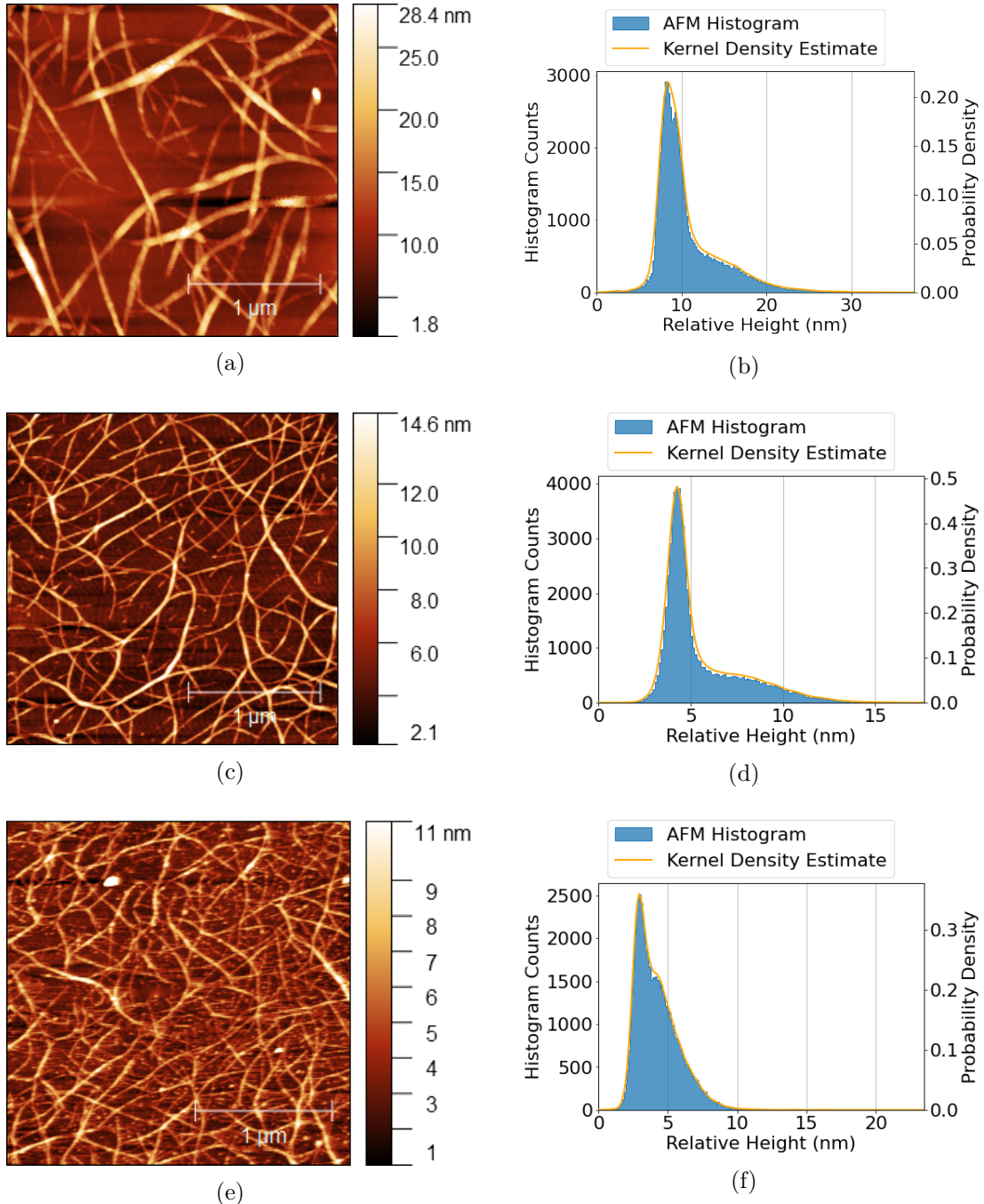


Figure 2.1.: $2.5 \mu\text{m} \times 2.5 \mu\text{m}$ atomic force microscope (AFM) images of carbon nanotube films deposited using various methods, shown side-by-side with histogram height distributions and kernel density estimate (KDE) plots corresponding to each image. The network shown in (a) with height distribution shown in (b) was deposited in solvent, the network shown in (c) with height distribution shown in (d) was dropcast in surfactant, and the network shown in (e) with height distribution shown in (f) was dropcast in surfactant with steam present.

2. Characteristics of Pristine Carbon Nanotube & Graphene Field Effect Transistors

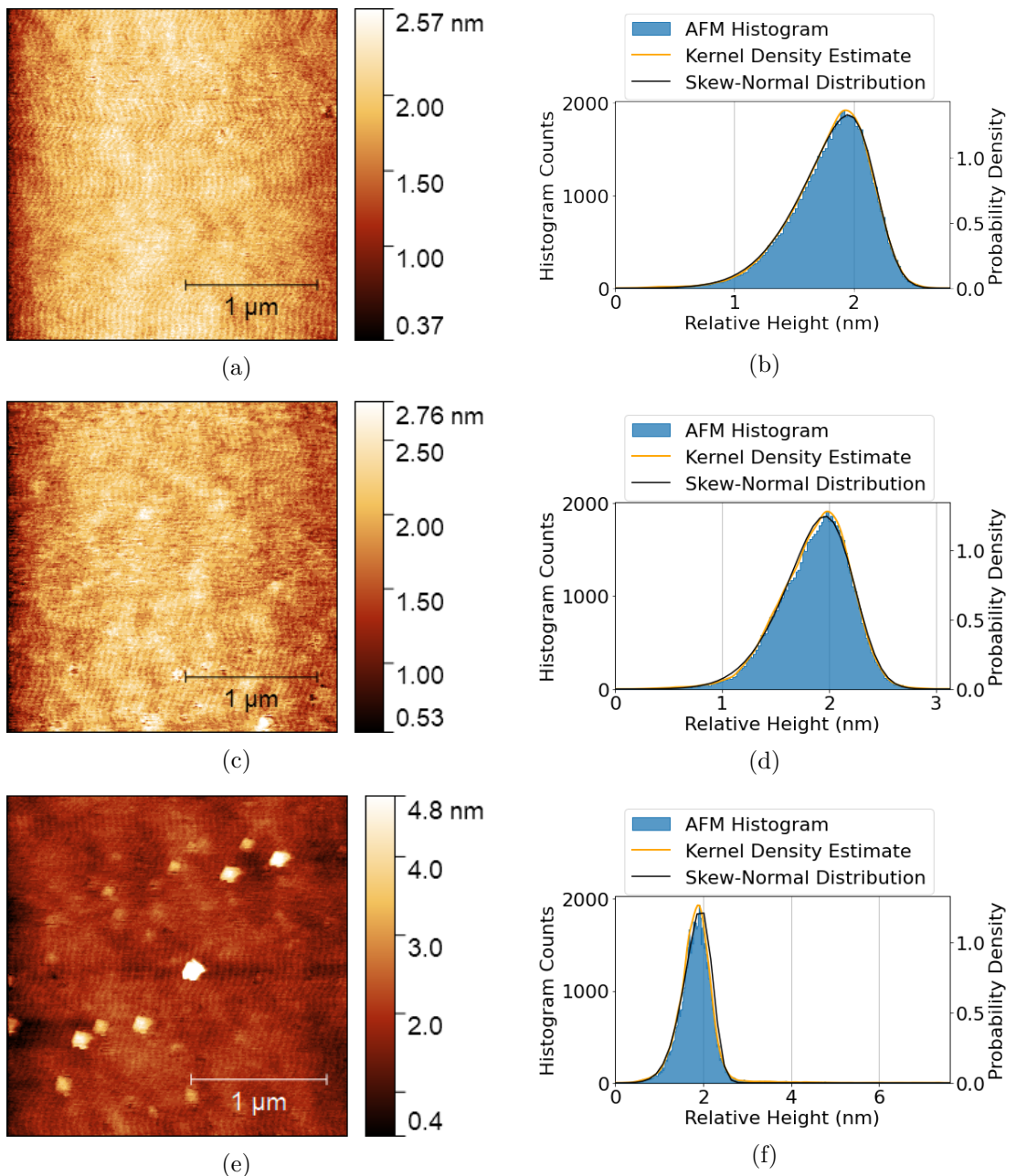


Figure 2.2.: $2.5 \mu\text{m} \times 2.5 \mu\text{m}$ atomic force microscope (AFM) images of silicon dioxide substrates alongside histogram height distributions and KDE plots corresponding to each image. The substrate in (a) and (b) was exposed to solvent, the substrate in (c) and (d) was exposed to surfactant, and the substrate in (e) and (f) was exposed to surfactant with steam present.

2.2. Carbon Nanotube Network Morphology and Composition

However, Figure 2.2f has a pronounced positive skew with a long tail. The tail appears to result from the contribution of residual surfactant aggregates to surface morphology, observed in Figure 2.2e and recently discussed elsewhere in the literature [17], [20]. Attempting to fit a skew-normal distribution to this histogram fails when all three variables are allowed to vary due to the presence of the tail. Instead, previous values obtained for ξ and ω can be used for the fitting process, with only α allowed to change. Fixing ξ and ω at 2.2 nm and 0.5 nm respectively gives the result shown in Figure 2.2f. The fitted distribution has an α of -2.4. The distribution closely fits the negative tail of the histogram, but deviates slightly from the positive tail due to the presence of surfactant. Since this deviation is small, the quality of the fit is still reasonably high, with an R-squared value of 0.98. Surfactant contamination could have negative effects on both sensitivity of carbon nanotubes and also could damage attached biological elements.

Using the morphology analysis technique outlined by Vobornik *et al.* [17], five successive diameter measurements of 30 carbon nanotube bundles were collected using Gwyddion. Measurements were not taken at bundle junctions. A height threshold ‘mask’ was defined in Gwyddion to determine average substrate height, as shown in Figure 2.3a. This background value was subtracted from our diameter measurements to determine the actual bundle height. The means of the solvent-deposited, surfactant-deposited and steam-assisted surfactant-deposited bundle diameter histograms are 8.8 ± 4.0 nm, 4.2 ± 1.8 nm and 3.3 ± 1.0 nm respectively. An increased maximum feature height leads to an increased mean background height, and by examining the AFM images in Figure 2.1 it appears this may be due to deep artifacts on the surface of the substrate in the vicinity of large features. The average of the five height-adjusted values for each carbon nanotube bundle was then calculated, and these 30 averages were sorted into six equal-sized bins. The binned bundle diameter measurements, alongside estimated probability density, are shown in Figure 2.3.

From Figure 2.3, it is clear that each histogram appears to follow a positively skewed normal distribution, different to the skew-free normal distribution expected from previous works [15]–[17]. The skew is likely another artifact from imaging the network with the atomic force microscope. The force of the atomic force microscope tip is known to cause larger bundles to undergo some degree of compression, and the resulting systematic underestimation of their height may be responsible for the distribution skewness [17]. The fitted skew-normal distribution in Figure 2.3b has $\alpha = 2.7$, $\xi = 4.3$ nm, $\omega = 5.9$ nm, the distribution in Figure 2.3c has $\alpha = 2.4$, $\xi = 2.2$ nm, $\omega = 2.6$ nm, and the distribution in Figure 2.3d has $\alpha = 3.6$, $\xi = 2.2$ nm and $\omega = 1.5$ nm. The probability density for the carbon nanotube bundle histogram drops to approximately zero at or before 0 nm, which is physically appropriate.

Warning: package 'kableExtra' was built under R version 4.3.2

2. Characteristics of Pristine Carbon Nanotube & Graphene Field Effect Transistors

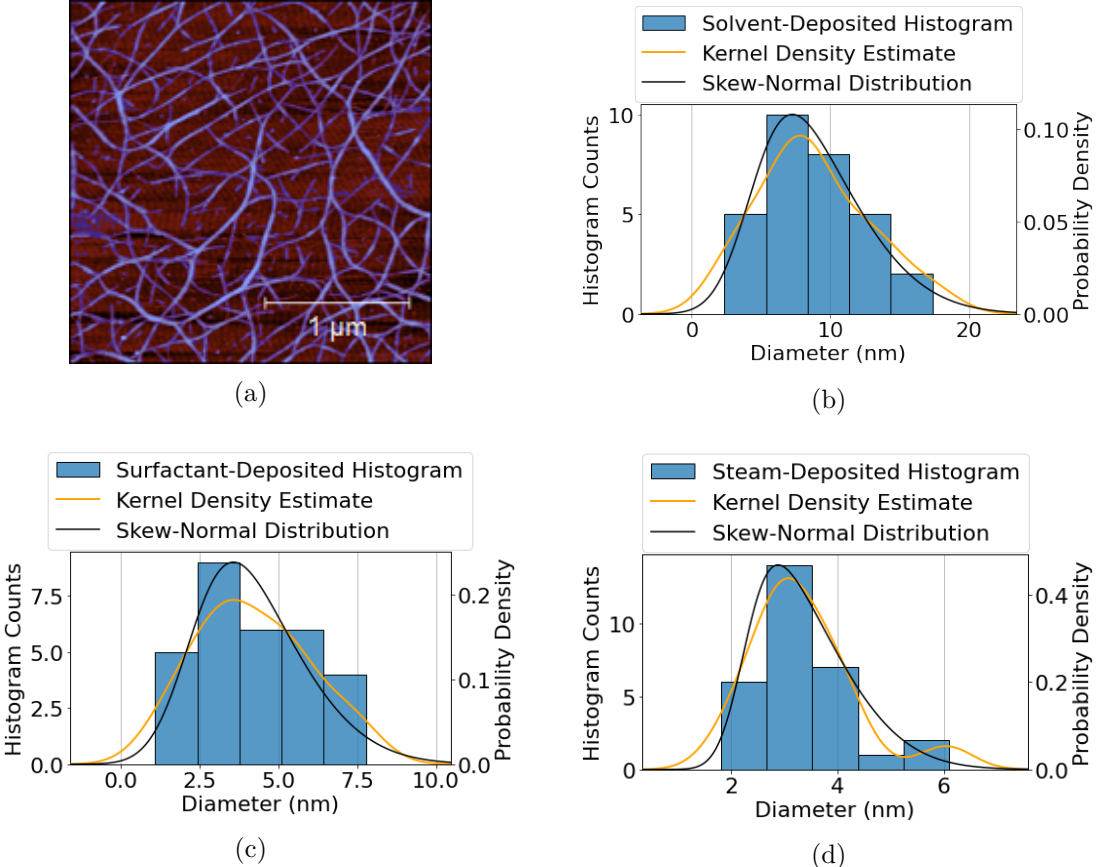


Figure 2.3.: An masked AFM image is shown in (a), where the masked carbon nanotube bundles are shaded blue. The mask sets a height threshold so that masked features are excluded from the height dataset. Histogram height distributions with corresponding KDE plots collected via the morphology analysis method outlined by Vobornik *et al.* [17] are shown in (b)-(d). The substrate in (b) was exposed to solvent, the substrate in (c) was exposed to surfactant, and the substrate in (d) was exposed to surfactant with steam present.

2.2. Carbon Nanotube Network Morphology and Composition

Table 2.1.: The first eight optimised ratios of 2D packed circle diameter to encompassing circle diameter, given to 3 s.f. (encompassing circle diameter = d , number of packed circles = n , approximate packed circle diameter = d_n).

n	2	3	4	5	6	7	8	9
d/d_n	2.00	2.15	2.41	2.70	3.00	3.00	3.30	3.61

Previously, analysis of the morphology of carbon nanotube networks has been simplified by assuming the component nanotubes are cylinders, follow 2D packing and are of equal diameter [7]. Table 2.1 shows the relationship between the diameter of a bundle of 2D packed cylinders and the constituent diameters of up to nine cylinders within that bundle. From looking up the relevant d/d_n packing ratios, and assuming an average carbon nanotube diameter of 1.45 nm, it is possible to use to find the approximate number of nanotubes n likely to be present in the mean bundle size corresponding to each deposition type [21], [22]. These estimates are shown in Table 2.2. Also shown in Table 2.2 is an estimate of the ratio of single- to multi-tube bundles for each deposition. This estimate was obtained by taking the integral of each distribution with a lower bound of 2.9 nm, the minimum multi-tube bundle size for 1.45 nm diameter nanotubes. As the area under the curve represents the probability a bundle will have a particular diameter, this integral should give a good estimate of the relative proportion of multi-tube bundles. Table 2.2 should be interpreted as lower-limit estimates of the size and relative proportion of bundles, recalling that the distribution skewness indicates underestimation of the true bundle height.

Table 2.2.: The mean of histogram distributions for carbon nanotube films deposited using various methods, alongside estimates for the number of nanotubes present per mean bundle and the estimated proportion of multi-tubed bundles present across the network.

	Mean Bundle Diameter (nm)	Tubes per Average Bundle	% Multi-Tube Bundles
Solvent deposited	8.8 ± 4.0	28	> 96%
Surfactant deposited	4.2 ± 1.8	5	> 75%
Surfactant deposited with steam	3.3 ± 1.0	3	> 65%

Both the carbon nanotube bundle diameter mean and standard deviation are small for surfactant-deposited films when compared to the mean and standard deviation of solvent-deposited films. However, despite the presence of surfactant, it is apparent both from Figure 2.1 and Table 2.2 that not all surfactant-dispersed carbon nanotubes are deposited individually. Bundling may occur during the process of deposition onto the

2. Characteristics of Pristine Carbon Nanotube & Graphene Field Effect Transistors

substrate, which could disrupt the repulsive forces from the surfactant coating and allow attractive forces to temporarily dominate. It is possible that the bundling of surfactant-dispersed carbon nanotubes is a consequence of dynamics introduced by the coffee-ring effect [23], [24]. The coffee-ring effect refers to a build-up of dispersed solid forming around the edges of a dispersion evaporating on a surface. This process occurs due to the dispersion edges being fixed by surface forces, leading to capillary flow outwards to replace liquid evaporating at the edges, bringing solid material along with it. The presence of vapour is known to disrupt this capillary effect [25], which may explain why mean bundle diameter is lower for the films deposited in surfactant with steam present relative to films deposited in surfactant without steam.

The discussion in this section gives us a new understanding of the histograms shown in Figure 2.1. It is now apparent that these histograms are linear combinations of skewed normal distributions. These distributions include a negatively-skewed distribution corresponding to the substrate surface and a positively-skewed distribution corresponding to the carbon nanotube bundles. X and Y junctions between overlapping nanotubes may also form a similarly skewed normal distribution as part of the full histogram [7]. The complete linear combination could be modelled mathematically in order to rapidly extract key parameters from atomic force microscope images [26], but implementing this approach is outside of the scope of this thesis. Another outcome of this discussion is awareness that carbon nanotube bundling within a network is lowered by the presence of surfactant during deposition. Introducing steam when depositing with surfactant lowers bundling even further, but also leads to residual surfactant pooling and attaching to the substrate surface. These results may both be explained by the presence of steam enabling surfactant to follow carbon nanotubes to the substrate surface, which keeps them from bundling during the attachment process. The unwanted persistence of surfactant means that higher temperature vacuum annealing may be required for robust biosensors [27].

2.2.2. Raman Spectroscopy

Raman spectroscopy was also used to analyse and compare the deposited carbon nanotube networks. Raman spectra were collected from a solvent-deposited carbon nanotube film and a steam-assisted surfactant-deposited film, both on silicon dioxide, in the manner described in [?@sec-raman-characterisation](#). These spectra were then processed using the Python script mentioned in Section B.3. For each location, spectra over two wavenumber ranges were collected. A peak corresponding to the silicon dioxide substrate, found in the range between 100 cm^{-1} and 650 cm^{-1} , was used as a reference peak for the normalisation of intensity across the wavenumber range between 1300 cm^{-1} and 1650 cm^{-1} . These normalised spectra are shown in Figure 2.4. In all spectra, a D-band comprising a single D-peak is observed at $\sim 1320\text{ cm}^{-1}$, and a G-band comprising two G-peaks, G^- and G^+ , is observed between $\sim 1525\text{ cm}^{-1}$ and $\sim 1650\text{ cm}^{-1}$. These features are characteristic of networks of semiconducting carbon nanotubes [28], [29].

2.2. Carbon Nanotube Network Morphology and Composition

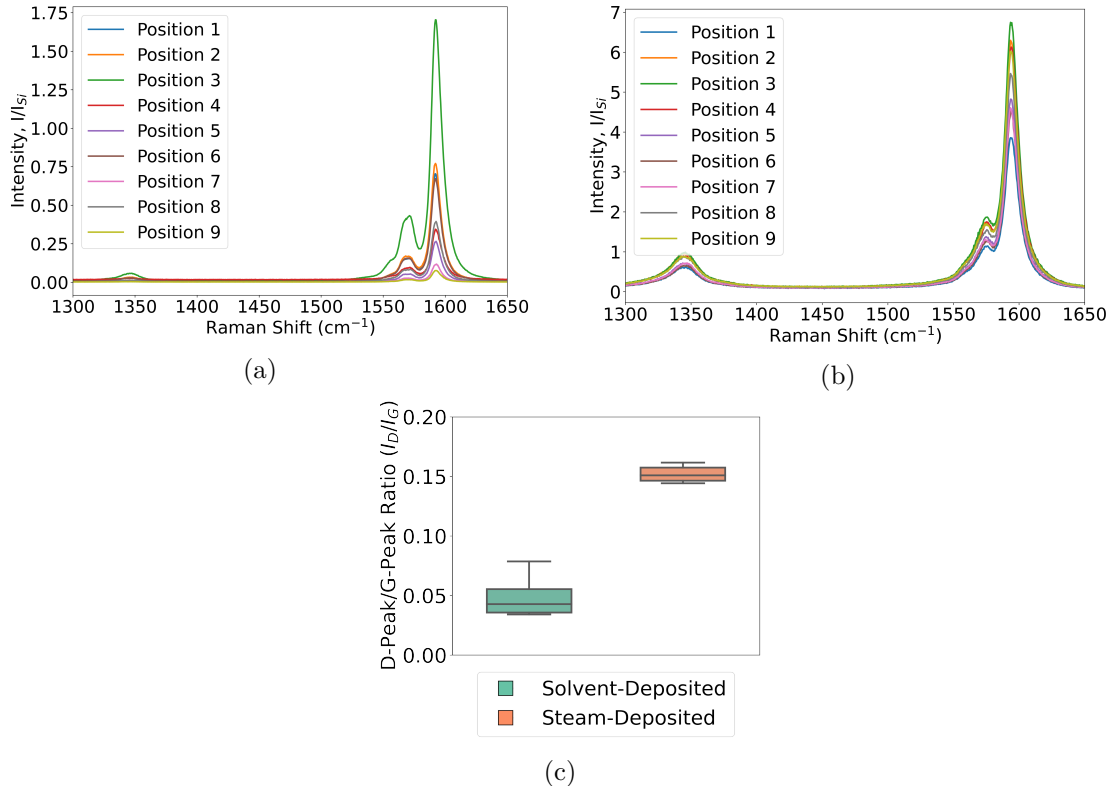


Figure 2.4.: A series of nine Raman spectra at different locations across a $40 \mu\text{m} \times 100 \mu\text{m}$ carbon nanotube film region, where (a) shows spectra from a film deposited using solvent while (b) shows spectra from a film deposited with surfactant in the presence of steam. (c) shows the spread of the D-peak/G⁺-peak spectral ratios corresponding to each film.

2. Characteristics of Pristine Carbon Nanotube & Graphene Field Effect Transistors

Closer inspection of the D peak and G peaks can give us important information about network composition. G^- is a minor peak found at $\sim 1570\text{ cm}^{-1}$, while G^+ is a larger feature at $\sim 1590\text{ cm}^{-1}$. The G^+ feature describes the in-plane vibration of carbon bonds along the length of the carbon nanotubes, while the G^- feature describes the in-plane vibration of bonds about the nanotube circumference [29], [30]. The splitting between the wavenumber location of the G^- and G^+ local maxima is lower in Figure 2.4b than in Figure 2.4a, indicating more metallic nanotubes are present in the surfactant-deposited network [30]. The D-peak gives an indication of the defects present in the carbon nanotube atomic structure [29], [30]. The size of the normalised D-peak appears much lower in Figure 2.4a than in Figure 2.4b, indicating the solvent deposition process introduces less defects to the carbon nanotubes than surfactant-mediated deposition.

It is also possible to compare the relative magnitude of the D-peak and G^+ -peak intensity to quantify carbon nanotube structural disorder, which disrupts in-plane lattice vibration [28], [29]. Figure 2.4c gives a summary of the ratios between the D-peak and G^+ -peak across all nine positions for the solvent-deposited and surfactant-deposited film. It is immediately observed that I_D/I_G is significantly larger for the steam-assisted, surfactant-deposited films than for the solvent-deposited films. This is a further indication of the presence of defects across the steam-deposited network. These defects are likely introduced through the introduction of charge impurities by surfactant aggregates present around the carbon nanotubes [20]. However, at the same time, the range of values for the I_D/I_G ratio is lower for the steam-deposited network. This spatially homogeneous vibrational behaviour implies the steam-deposited network is more evenly distributed than the solvent-deposited network, which matches the discussion in Section 2.2.

2.3. Electrical Characteristics of Pristine Devices

2.3.1. Python Analysis

Analysis of electrical measurements was performed using the three modules described in Section B.4. The first of the three modules is for processing sensing datasets. This module cleans, analyses and filters sensing data and produces a variety of plots. These plots include normalised plots (type of normalisation can be set in the code config file), plots with fitted curves, plots with the linear baseline drift removed, plots of signal with analyte addition, “despiked” plots and “filtered” plots. The analysis used to produce these plots is described further below. It is possible to add annotations to any of these plots using the config file, and it is possible to produce a plot with a combination of these modifications. The module can also fit exponential and linear trendlines to regions of the sensing data, and find the signal change per analyte addition; the module then returns spreadsheets containing the results of these analyses, including the standard deviation for all calculated parameters.

2.3. Electrical Characteristics of Pristine Devices

The `scipy.optimize.curve_fit` function is used in the first module to fit linear and exponential curves to regions of interest of the sensing data. For a linear fit $mt + b$, initial parameters are simply set as $m = 1$ and $b = 0$. For an exponential fit $a \exp(-t/\tau) + c$, rough approximations are used for the initial parameters: c is set as the final current measurement of the region of interest, a is set as the initial current measurement minus c , and τ is set as the time where current has dropped to $e^{-1}a + c$.

“Despiked” plots have had spurious datapoints removed through the use of an interquartile range rolling filter. The window size of the rolling filter used was 40 datapoints, and datapoints in each window with a z-score above ± 3 were removed from the plotted/processed data. “Filtered” plots had noise reduced using a moving median filter. The moving median filter is more effective at removing noise than a simple moving average, and has advantages over other filters (such as the Savitzky-Golay filter) when removing noise from data with sharp edges, as is the case for sensing data. Median filtering can also be used for baseline drift compensation, though this approach was not used in this thesis [31]. The moving median filter used had a window of 40 datapoints.

Plots of signal with analyte addition were constructed from current data after first removing baseline drift and applying a moving median filter. A simple difference calculation between the mean of the filtered current before an addition and the mean of the filtered current after the addition was performed at each addition. These differences were then normalised relative to the initial current. The signal with analyte addition give reasonably consistent results regardless of whether baseline drift was removed from the data, as shown in Figure 2.5. We can therefore be confident that robust signal with analyte addition plots are robust even in the presence of significant drift.

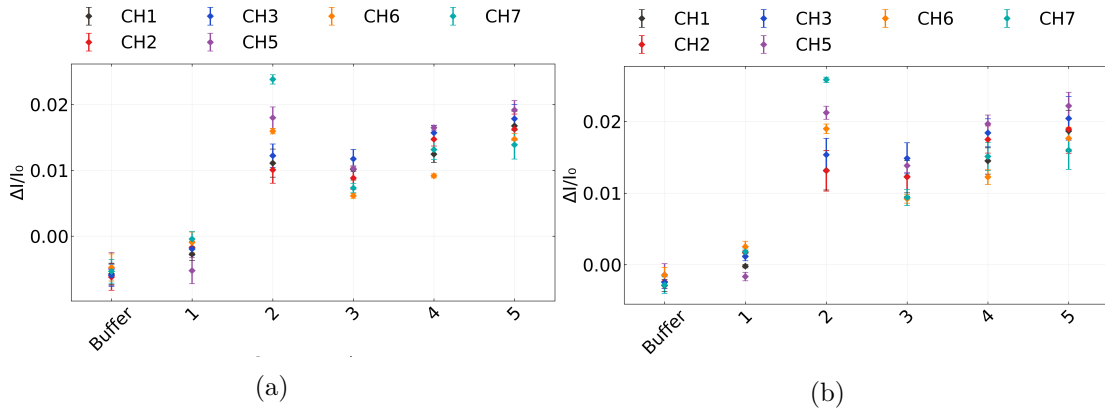


Figure 2.5.: A comparison of signal with analyte addition plots taken from the same salt concentration sensing dataset (the same dataset as used in Figure 2.11). In (a), a simple difference calculation performed on filtered data was used, while in (b) the same calculation was performed on filtered data with the baseline drift removed, the method used in the body of the thesis.

The second module creates combined and individual plots of transfer data collected

2. Characteristics of Pristine Carbon Nanotube & Graphene Field Effect Transistors

from eight channels on a single device. In combined plots, channels which are non-working, due to being shorted or non-conducting, are removed via setting a maximum and minimum possible on-current in the config file. Various parameters from the transfer characteristics are saved as a spreadsheet along with standard error. These parameters include on current, off current, subthreshold slope and threshold voltage for the carbon nanotube devices, and on current, off current and major Dirac point voltage for graphene devices. The device type being analysed can be set in the config file.

The third module allows for comparison of transfer measurements taken of the same channel before and after some modification. It also calculates the shift in either threshold voltage or major Dirac voltage of the device.

2.3.2. Carbon Nanotube Network Devices

Each carbon nanotube device fabricated was electrically characterised as described in **?@sec-electrical-characterisation**, and electrical data was analysed using the Python code discussed in Section B.4. Devices with a 100 nm or 300 nm SiO₂ layer were used for liquid gated measurements, and devices with a 100 nm SiO₂ layer were used for backgated measurements. Figure 2.6 displays multi-channel measurements of representative devices fabricated as described in **?@sec-fabrication**. To ensure a consistent comparison, each device here was encapsulated with AZ® 1518 encapsulation before measurements were taken. The channels which did not exhibit reliable transistor characteristics are not shown. These ‘non-working’ channels were either shorted, due to metal remaining on the channel after lift-off, or were very low current, due to a very sparse carbon nanotube network. Devices shown here with a solvent-deposited carbon nanotube network were fabricated prior to Jan 2022; devices with a surfactant-deposited network without steam present were fabricated prior to Jun 2021; devices with a surfactant-deposited network without steam were fabricated prior to Sep 2022.

Liquid-Gated CNTFETs

The liquid-gated devices in Figure 2.6a, Figure 2.6c and Figure 2.6e each exhibited ambipolar characteristics, commonly observed in liquid-gated carbon nanotube network FETs [7], [32]–[36]. When devices were appropriately configured, leakage current (shown by the dashed traces) did not exceed $\sim 1 \times 10^{-7}$ V across the forward and reverse sweep. The devices shown which used steam-deposited carbon nanotube films showed the least hysteresis. Section 2.2.1 demonstrates that the mean diameter of the bundles in these films is about 0.9 nm less than the mean bundles in films deposited without steam present, and 5.5 nm less than those in films deposited in solvent. Hysteresis is known to scale roughly linearly with bundle diameter, due to trapped charge increasing as bundle density of states is increased [37]. Steam-deposited devices also showed significantly less channel-to-channel variation in electrical characteristics more generally. Channel 1 in Figure 2.6a has a much higher off-current than the other channels of the same device,

2.3. Electrical Characteristics of Pristine Devices

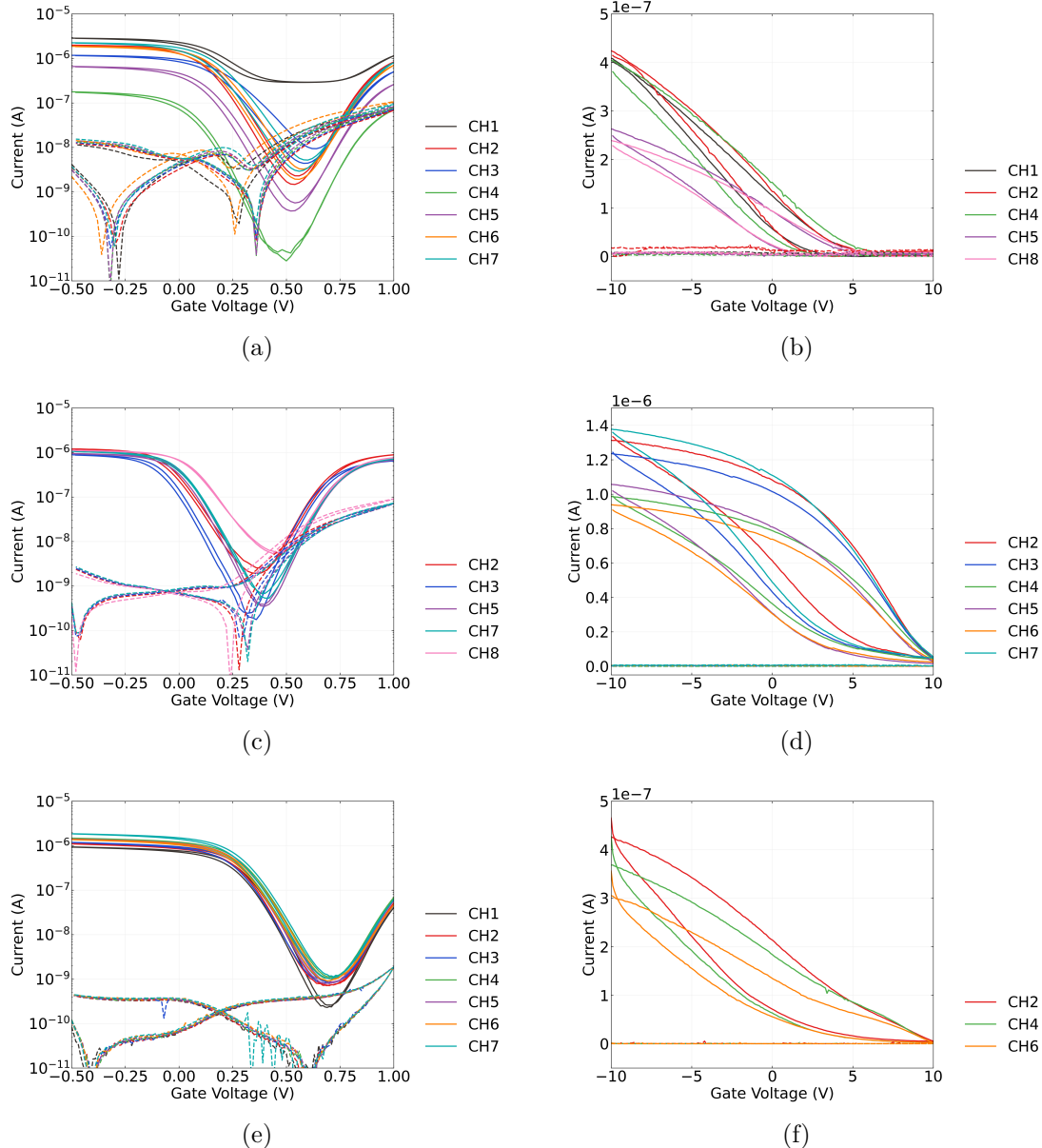


Figure 2.6.: Liquid-gated (left) and back-gated (right) transfer characteristics of AZ® 1518 encapsulated field-effect transistors, where the film was deposited with solvent in (a) and (b), deposited with surfactant in (c) and (d), and deposited with surfactant in the presence of steam in (e) and (f). A step size of 100 mV was used for the backgated sweeps in (a), (c) and (e), while a step size of 20 mV was used for the liquid-gated sweeps in (b), (d) and (f). Gate current (leakage current) is shown with a dashed line. The source-drain voltage used for all sweeps was $V_{ds} = 100\text{mV}$, and 1XPBS was used as the buffer for the liquid-gated measurements here.

2. Characteristics of Pristine Carbon Nanotube & Graphene Field Effect Transistors

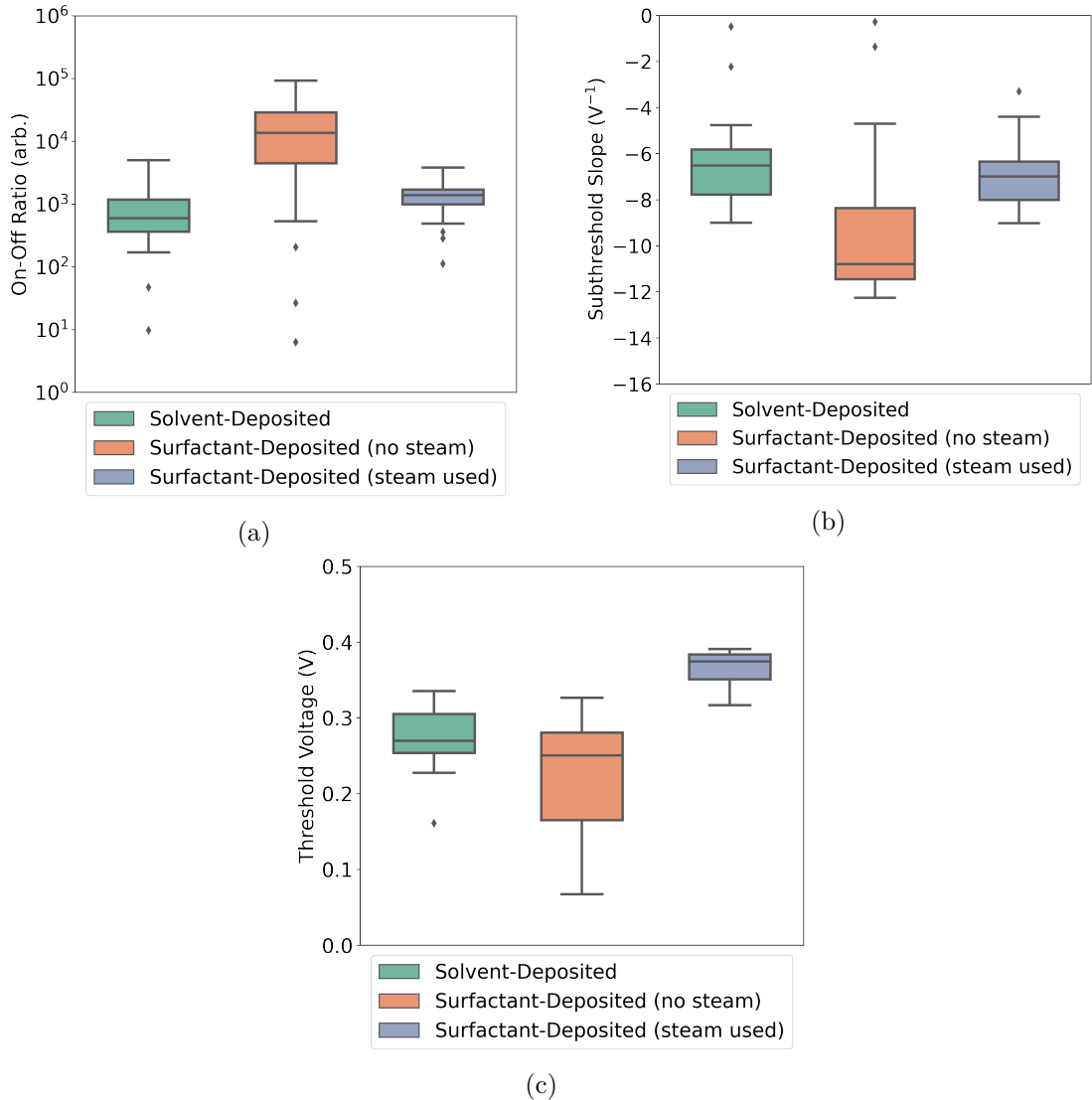


Figure 2.7.: These boxplots illustrate the statistical distribution of (a) the on-off ratio, (b) the subthreshold slope, and (c) the threshold voltage of AZ® 1518 encapsulated liquid-gated transistor channels corresponding to each type of carbon nanotube film deposition. For each deposition type, electrical characteristics were taken of 21 channels of at least three separate devices. The boxes indicate the 25th and 75th percentile of the distribution.

2.3. Electrical Characteristics of Pristine Devices

which appears to be due to a uncommonly high proportion of metallic carbon nanotubes present in the network conduction pathways of this channel [38], [39].

A summary of key parameters of pristine liquid-gated devices is shown in Figure 2.7. The full dataset consists of three sets of 21 liquid-gated transfer characteristics of working channels, with each set corresponding to the use of a particular method of carbon nanotube network deposition in the device fabrication. Measurements from at least three devices are included in each set. Each entry in the summary corresponds to the average of the specific parameter in the forward and reverse sweep direction. When steam was used for surfactant deposition of films, the resulting devices showed highly consistent channel-to-channel electrical properties. Since the carbon nanotube films on these devices are relatively dense, as seen in Figure 2.1e, the network should be well above the percolation threshold. As many carbon nanotube pathways connect across the channel in parallel, small variations in the network morphology have less of an impact on the overall channel behaviour [7]. Figure 2.3 and Table 2.2 indicate that the range of bundle sizes is relatively low in the steam-deposited films used in these devices, meaning the electrical behaviour of dominant conduction pathways is more spatially consistent. The repeatable subthreshold regime behaviour between channels seen for steam-deposited devices is a desirable attribute for reliable real-time multiplexed biosensing [32], [33], [40].

Channels from surfactant-deposited film devices usually showed a larger on-off ratio and subthreshold slope than those from solvent-deposited devices. Decreasing the ratio of gate-sensitive semiconducting carbon nanotubes to metallic nanotubes tends to decrease the on-off ratio [7], [15], [38], [39]. Section 2.2.2 seems to indicate there are more metallic nanotubes present in the surfactant-deposited films than in the solvent-deposited films. However, percolating conduction pathways dominate device behaviour and nanotube pathways across the channel with a lower degree of bundling are less likely to contain metallic tubes [7]. Therefore, the larger on-off ratio for surfactant-deposited film devices is likely a result of their reduced nanotube bundle size and reduced bundle size variation relative to other films, as discussed in Section 2.2. The larger subthreshold slope is likely due to increased mobility from a denser nanotube network in surfactant-deposited films [38], as seen in Figure 2.1e. A larger on-off ratio and subthreshold slope results in a larger change in conductance in response to changes in the transfer characteristic curve. Therefore, the larger on-off ratio and subthreshold slope of steam-deposited devices is desirable for improved sensor performance [32], [33], [40].

All channels characterised had a positive threshold voltage (V_{th}). The threshold voltage was largest and most consistent for steam-assisted surfactant-deposited films. The relatively high values of V_{th} which correspond to channel measurements from steam-assisted surfactant-deposited devices indicates increased *p*-doping of the network relative to networks deposited via alternative processes [7], [41], [42]. As seen from Figure 2.2e-f and Figure 2.4c, the steam deposition process leads to the presence of significant, persistent surfactant aggregates. It has been previously established that residual surfactant can *p*-dope carbon nanotubes, alongside enhancing *p*-doping from adsorbed oxygen and water

2. Characteristics of Pristine Carbon Nanotube & Graphene Field Effect Transistors

[20], [27], [43]. The presence of residual surfactant may also explain the lowered sub-threshold slope, and therefore mobility, of the steam-deposited devices relative to devices with films deposited in surfactant without steam. The analysis by Kane *et al.* shows that the thermal annealing at 150°C used in this work to remove residual surfactant is likely inadequate for this purpose. Oxidation of devices and vacuum annealing at high temperatures ($> 600^\circ\text{C}$) may be required for effective desorption of the persistent surfactant [27], [44]. Devices using films made using the alternative two methods have the advantage of not requiring careful treatment to remove surfactant.

Back-Gated CNTFETs

When characterising devices using the vapour delivery system chip carrier, the setup arrangement meant all measurements were taken using a backgate. Figure 2.6b, Figure 2.6d and Figure 2.6f show that backgated devices exhibit *p*-type transistor behaviour. Gate current leakage was negligible, as shown by the dashed line staying close to zero across the sweep. Significant hysteresis was observed. The hysteresis can be explained by the presence of defects or charge traps within and on the surface of the silicon dioxide and at interfaces between the silicon dioxide and carbon nanotubes [45]–[47]. The hysteresis observed was much greater than for the corresponding liquid-gated sweeps on the right. The devices fabricated with a solvent-based deposition were switched off at a lower voltage than the devices which used surfactant during deposition.

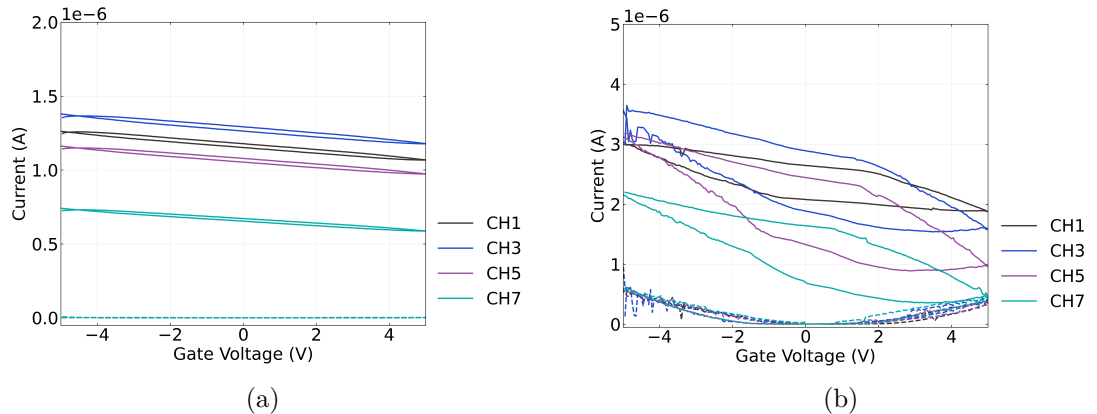


Figure 2.8.: Backgated transfer sweeps were taken of an single unencapsulated device with a 300 nm SiO_2 layer and steam assisted surfactant-deposited carbon nanotube network channels before and after being covered in 50 μL 1XPBS electrolyte.

Transfer measurements were taken to determine whether backgated measurements could be taken of an unencapsulated device in the vapour sensor chamber with 1XPBS covering the channels. Figure 2.8 shows the behaviour of an unencapsulated backgated device with a 300 nm SiO_2 layer before and after being covered by 50 μL of 1XPBS (phosphate

2.3. Electrical Characteristics of Pristine Devices

buffered saline). The on-off ratio and hysteresis of the channels increase significantly. The presence of water increases hysteresis through introducing charge traps at the silicon dioxide surface around the carbon nanotubes and at the surface of the nanotubes themselves [45], [47]–[49]. There is also a significant increase in current leakage to the backgate for larger applied voltages, despite the electrolyte having no visible physical contact with the silicon backgate or copper plane. This leakage current may simply be due to an increase in relative humidity around the device due to the presence of water [50]. As any variation in threshold voltage due to hysteresis and significant leakage current are undesirable for sensing procedures, this configuration was not used for vapour sensing purposes.

2.3.3. Graphene Devices

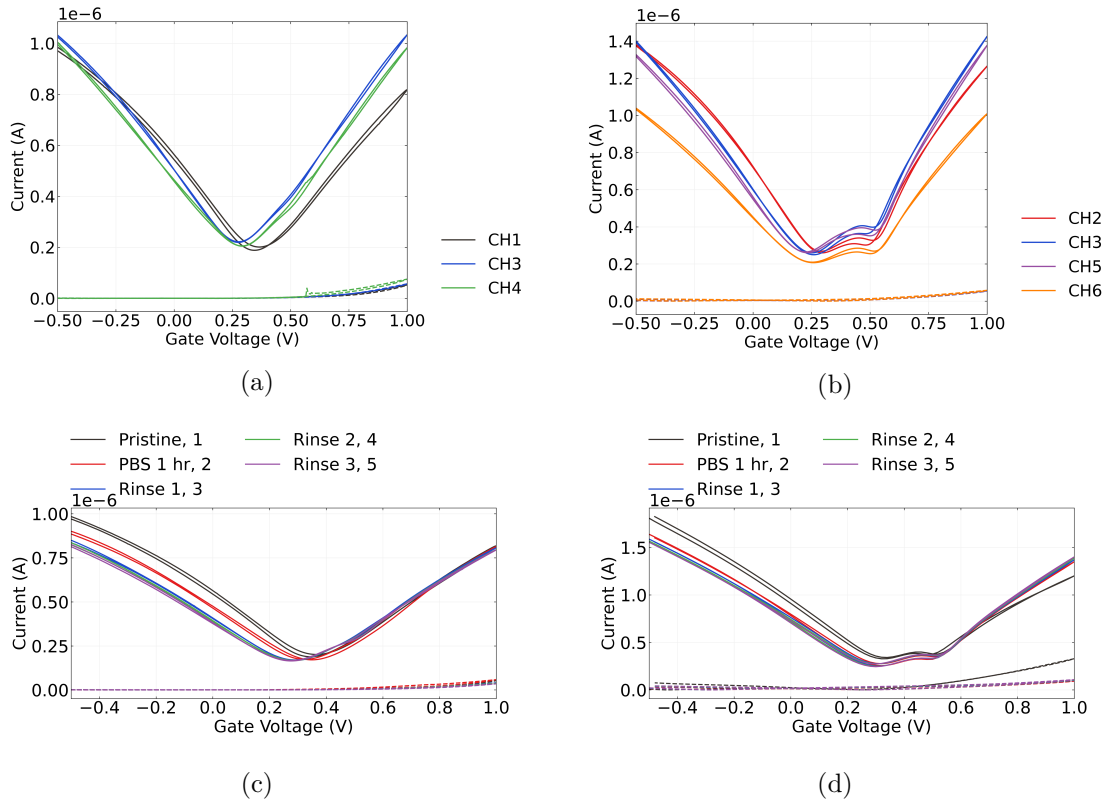


Figure 2.9.: These figures show liquid-gated transfer characteristics of channels from two AZ® 1518 encapsulated graphene devices. The characteristics of working device channels upon initial exposure to 1XPBS are shown in (a) and (b). The transfer characteristics of channel 1 in (a) and channel 5 in (b) after various degrees of exposure to 1XPBS are shown in (c) and (d) respectively, with each transfer sweep numbered in the order the sweeps were taken. The dashed lines correspond to measurements of gate leakage current.

2. Characteristics of Pristine Carbon Nanotube & Graphene Field Effect Transistors

Graphene field-effect transistor devices were electrically characterised in the manner described in ?@sec-electrical-characterisation and analysed using the Python code discussed in Section B.4.

Figure 2.9 shows the liquid-gated transfer characteristics of two graphene devices. These devices were fabricated prior to Jun 2021. Both devices exhibit the ambipolar characteristics typical of liquid-gated graphene devices [51]–[54]. As with the carbon nanotube network devices, leakage current remained below $\sim 1 \times 10^{-7}$ V across both the forward and reverse sweep. Hysteresis between the forward and reverse sweep is caused by trapping of charge within and on the surface of the SiO_2 dielectric [55]. The major Dirac point for these devices is slightly to the right of $V_{\text{Dirac}} \approx 0$ V, which indicates *p*-doping of the channel. This slight *p*-doping is likely a result of a adsorption of oxygen and water from the air and residue resist from photolithography [54], [56], [57].

Some devices exhibited a double-minima feature, indicating the presence of two Dirac points. This effect arises due to doping of graphene by the metal contacts. In shorter length channels, metal doping affects the entire channel length, leading to a consistent Fermi level and a single Dirac point. However, for longer channel lengths like ours, the doping effect from metal contact no longer reaches the entire channel, leading to a difference in Fermi level between the graphene in the channel and graphene under the metal contact. The difference in Fermi levels results in the presence of a second Dirac point [55], [58], [59]. The global minimum of the transfer characteristic can be referred to as the ‘major’ Dirac point.

Figure 2.9 also shows the effect of 1XPBS on the graphene channels. The channels were measured on exposure to 1XPBS, after exposure to 1XPBS for one hour, and after the device surface was rinsed and 1XPBS was replaced in the well one time, two times and three times successively. A slight negative shift of the major Dirac point was observed. This effect is possibly a result of gate bias stress, where successive transfer sweeps introduce charge traps to the graphene layer and alters the current level at a given gate voltage [60], [61]. Alternatively, Kireev *et al.* found that a series of liquid-gated sweeps also reduced the size of the second Dirac point, and suggested that it indicated the gate current was removing atmospheric contaminants from the graphene surface via current annealing [54]. This could be explained as the removal of contaminants causing improved contact between the metal and graphene surface, and thus increasing metal doping and consistency of the Fermi level across the channel. If the contaminants removed are *p*-dopants, then this effect could also explain the negative shift of the major Dirac point.

2.4. Aqueous Sensing of Phosphate Buffered Saline Concentration

Table 2.3.: Average on-off ratio and major Dirac point voltage for AZ® 1518 encapsulated liquid-gated graphene transistor channels at various stages of exposure to 1XPBS. Electrical characteristics were taken of 6 channels total, three channels from each of two devices.

	1XPBS: Initial	1XPBS: After 1 hr	1XPBS: Rinse
On-Off Ratio (arb.)	5.1 ± 0.3	5.0 ± 0.7	5.0 ± 0.6
Dirac Point Voltage (V)	0.28 ± 0.04	0.31 ± 0.03	0.28 ± 0.02

Table 2.3 shows the on-off ratio and major Dirac point voltage of the graphene devices. Apart from the previously-mentioned slight negative shift of the major Dirac point, these values were highly consistent before and after exposure to 1XPBS.

2.4. Aqueous Sensing of Phosphate Buffered Saline Concentration

2.4.1. Control Series and Baseline Drift

Table 2.4.: The threshold voltages V_{th} of each working channel of a steam-deposited device, and the difference between each V_{th} and the mean device threshold voltage $V_{th,mean}$.

Channels	CH1	CH2	CH3	CH5	CH6	CH7
Threshold voltage (mV)	160	150	130	140	180	140
Relative to mean (mV)	10	0	-20	-10	30	-10

To verify the sensitivity of the fabricated field-effect transistors and therefore verify their suitability for sensing, control measurements replicating a typical sensing experiment were taken before functionalising the device channels. This involved first ensuring the device showed no response to 1XPBS, a sequence referred to here as the ‘PBS control series’. The PDMS well contained 80 μL 1X PBS at 0 s. The PBS control series ran over the first 1800 s, with 20 μL phosphate buffer saline (1XPBS) additions at 100 s, 200 s and 300 s, and 20 μL subtractions at 400 s, 500 s and 600 s. The device was left untouched over the next 1200 s to allow the current level to settle. The gate voltage was held at $V_g = 0$ V.

Figure 2.10a shows the transfer sweeps of the six working channels of a steam-assisted surfactant-deposited carbon nanotube field-effect transistor encapsulated with AZ® 1518, fabricated in Mar 2023 and measured using the PXIE. The central ‘negative

2. Characteristics of Pristine Carbon Nanotube & Graphene Field Effect Transistors

current' feature in the transfer characteristics of channels 1 and 7 is due to unphysical measurements which come from equipment error and can be treated as zero current passing through the channel. The threshold voltages of the channels are shown in Table 2.4. Table 2.4 also shows the difference between the threshold voltage of each channel and the mean threshold voltage of the device. The mean threshold voltage was $V_{th} = 150 \pm 20$ mV. As discussed previously, the electrical characteristics are highly consistent between the channels due to the film deposition method used.

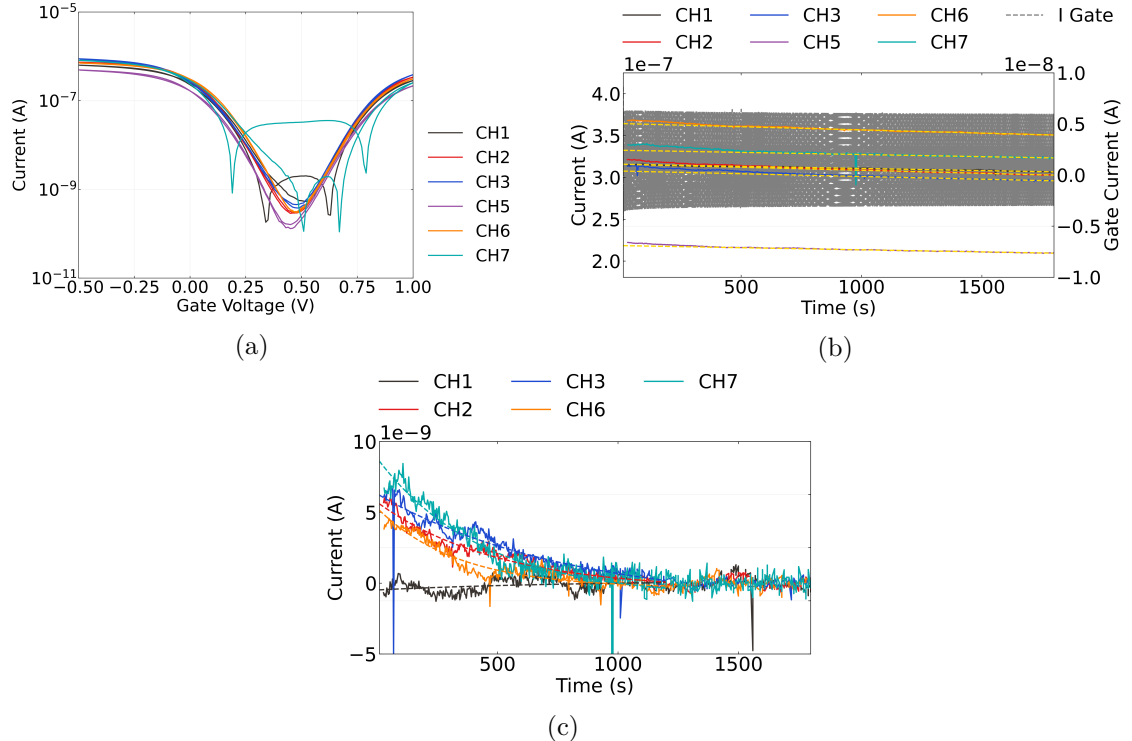


Figure 2.10.: The transfer characteristics in (a) were taken of the steam-deposited carbon nanotube field-effect transistor used here for an example of salt concentration sensing. The absolute values of measurements are shown, so that negative values resulting from measurement error can be visualised. Linear fits to the PBS control series from each channel from 1200 s onwards are shown in (b), while exponential fits to the PBS control series from 0 – 1200 with the linear fit subtracted are shown in (c). No significant response to PBS additions are seen at any of the addition times from 100 s - 600 s.

Figure 2.10b shows the PBS control series corresponding to each device channel alongside gate current. In both series, there is no clear stepwise response to any addition or subtraction of 1XPBS. Gate leakage current remains negligible across the entire control series, with no change in response to 1XPBS additions. The current has a period of faster decay followed by slower baseline drift, similar to observations by Lin *et al.* and more recently Noyce *et al.* for parallel arrangements of single carbon nanotubes in

2.4. Aqueous Sensing of Phosphate Buffered Saline Concentration

air or vacuum [61], [62]. This effect results from changes in the occupancy of charge traps in and around the substrate and carbon nanotubes. The magnitude of baseline drift is lower for our devices than for those characterised by Noyce *et al.*, which may be a result of numerous device and setup differences which affect the presence of charge traps. These differences include liquid-gating instead of back-gated, the use of a network of carbon nanotubes instead of single nanotubes, a different channel length, the use of a 300 nm instead of 90 nm SiO₂ layer, and the use of an asymmetric, liquid-gated transfer sweep over a shorter voltage range to characterise devices before each control series was measured [61].

Table 2.5.: The coefficients of linear fits to the PBS control series of each channel between 1200 – 1800 s, where m is the gradient and b is the constant term.

Channels	CH1	CH2	CH3	CH5	CH6	CH7
c_1 (pA/s)	-5.1±0.2	-7.2±0.1	-6.5±0.1	-5.0±0.1	-7.6±0.1	-5.1±0.2
c_2 (μ A)	0.316	0.316	0.308	0.218	0.364	0.332

Table 2.6.: The coefficients of exponential fits to the PBS control series of each channel between 0 – 1200 s, after the linear fit has been subtracted, where a is the gradient and τ is the time constant.

Channels	CH1	CH2	CH3	CH6	CH7
A (nA)	-0.66 ± 0.26	6.21 ± 0.09	7.84 ± 0.41	5.67 ± 0.11	9.82 ± 0.47
τ (s)	800 ± 750	500 ± 30	790 ± 100	330 ± 20	440 ± 70

As a first approximation to the longer time constant exponentials discussed by Noyce *et al.* [61], linear fits were performed on each PBS control series from 1200 – 1800 s. These linear fits are shown by the dashed yellow lines in Figure 2.10b. The parameters from each fit in Figure 2.10b are shown in Table 2.5, where $I = c_1 t + c_2$. The fits for channels 1, 5 and 7 are all in parallel within error. The gradient value for each fit in Figure 2.10b is reasonably consistent between all channels, all falling within a 2.6 pA/s range. When the long-term linear fits were subtracted from the raw data, the remaining dataset followed a exponential decay trend for both control series. Figure 2.10c shows exponential fits to the remaining curve from 0 – 1200 s, which was successful for all channels except channel 5. The parameters from each fit are shown in Table 2.6, where $I = A \exp(-t/\tau)$. The exponential fits had characteristic time constants τ ranging between 300 – 800 s, indicating that 1800 s is a sufficient length of time for this short-term baseline drift to completely decay to zero. The exponential term for channel 1 is close to linear, indicating the channel has low net trapped charge. It is unclear why the behaviour of this channel is significantly different from the others.

2. Characteristics of Pristine Carbon Nanotube & Graphene Field Effect Transistors

From this analysis it appears that the baseline drift for the liquid-gated carbon nanotube devices can be accurately approximated as a combination of a exponential and linear term. The lack of response to 1XPBS at any of the six PBS addition and removal times gives us confidence that this is a stable baseline which can be used for reliable chemical sensing. Furthermore, after ~ 800 s the baseline drift can be reasonably approximated as linear, with a small gradient of less than -10 pA/s. The slow change of current means that it becomes easier to distinguish responses due to analyte addition. It can therefore be concluded that the 1800 s length of the PBS control series is appropriate for minimising baseline drift for more reliable sensing.

2.4.2. Sensing Series

A salt concentration sensing series were performed from 1800 s onwards, directly after the PBS control series. The responses to successive dilutions of the liquid-gate electrolyte were recorded to confirm the fabricated devices were sensitive to small environmental changes in their pristine state, to check for spurious signals, and to ensure gate current leakage or other confounding factors were not contributing to sensing responses. The PDMS well contained 80 μL 1X PBS at 1800 s. During the series, successive additions of deionised water were made to reduce the concentration of PBS in the well. An initial 1X PBS addition was performed at 2100s, to confirm no changes occurred during the PBS control series that would interfere with sensing. All additions to the well in the sensing series and resulting changes to the PBS concentration in the well are shown in Table 2.7.

Table 2.7.: This table shows the times at which 20 μL additions were made to the PDMS well, with 300 s between each addition. The concentration in the well after each addition and the change in concentration after each addition are also shown. The well contained 80 μL of 1X PBS at 1800 s.

	1X PBS Addition	DI Water Additions				
Time (s)	2100	2400	2700	3000	3300	3600
Final PBS volume (μL)	100	120	140	160	180	200
Final PBS concentration	1X	0.83X	0.71X	0.63X	0.56X	0.50X
Δ PBS concentration	0	-0.17X	-0.12X	-0.09X	-0.07X	-0.06X

Figure 2.11a shows a multiplexed salt concentration sensing series from the channels of a single AZ® 1518 encapsulated device, measured with the NI-PXIe. The gate voltage used was 0 V, which meant current measurements were well above the magnitude of the subthreshold device current. Gate current measurements did not exceed 1 nA for the SU8 encapsulated devices, and did not exceed 10 nA for the AZ® 1518 devices. At each of the deionised water addition times, the current traces for at least two out of

2.4. Aqueous Sensing of Phosphate Buffered Saline Concentration

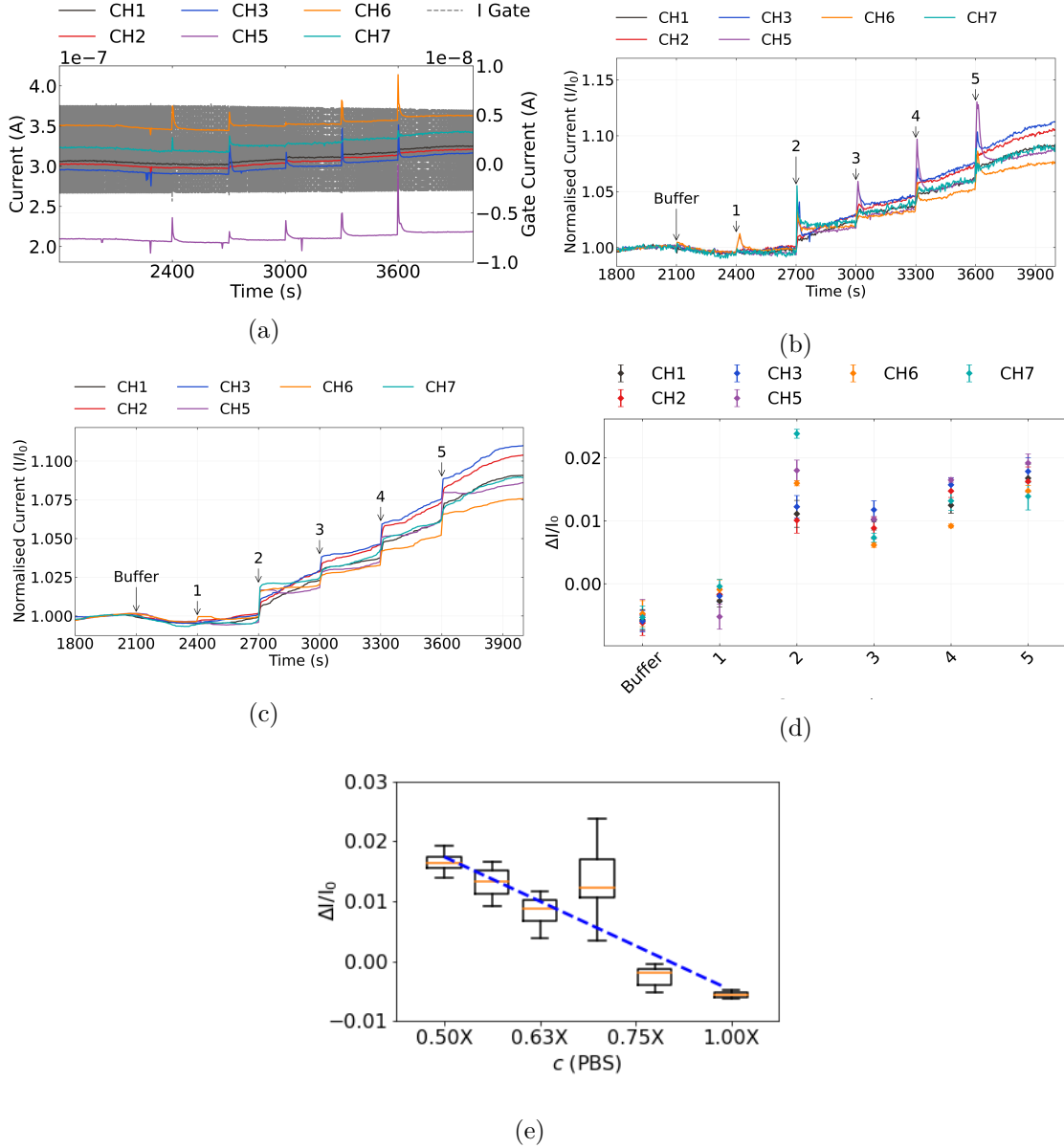


Figure 2.11.: Various visualisations of a multiplexed salt concentration sensing series taken from a single device. The source-drain voltage V_{ds} was 100 mV, and gate voltage V_g was 0 V. In (a), the raw current measurements for each channel are shown alongside gate current. The same measurements after despiking, removal of baseline drift and normalisation to initial current are shown in (b), (c) shows the data in (b) after being processed with a moving median filter, and (d) shows the signal changes in (c). The signal data in (d) is shown in box plot format in (e) alongside a fit to the median change in signal for each addition. The R squared value for the fit was 0.86.

2. Characteristics of Pristine Carbon Nanotube & Graphene Field Effect Transistors

six channels showed a sharp, transient increase in current followed by a return to an increased baseline. It is well established that changing the salt concentration of the liquid gate has an electrostatic gating effect on the carbon nanotubes or graphene, and changes the transfer characteristics of the channel. This shift in transfer characteristic leads to a real-time signal response to each addition [33], [52], [54].

Using the data in Table 2.5, the linear term approximating baseline drift (mt) for each channel can be subtracted from the data in Figure 2.11a to account for the downward drift. The mean current level just before 1800 s then becomes roughly constant. Next, each channel is normalised relative to their initial mean current level I_0 . Artifacts resulting from PXIE-2737 module lag, single datapoints which fall well below the current level of the immediately preceding and succeeding datapoints, are also removed. This ‘despike’ process uses an interquartile range filter, which is described in Section B.4. The resulting dataset is shown in Figure 2.11b. This figure shows that the signal-to-noise ratio remains roughly similar across all channels of the device. However, the behaviour of the initial transient increase with each addition is highly variable across channels and between additions for a single channel.

As measurement of the highly variable initial transient is not useful for robust sensing purposes, a moving median filter was applied, with the implementation of this filter discussed in Section B.4. The filtered data is shown in Figure 2.11c. Noise and initial transients are removed completely, while the clearly defined step to a new current baseline is retained. Using the realtime data in Figure 2.11c, a plot of signal against addition can be created using the method described in Section B.4, shown in Figure 2.11d. This presentation of the data allows us to see the increase at each step relative to I_0 .

Intriguingly, even though the largest change in PBS concentration occurred at the first deionised water addition (see Table 2.7), there was very little signal change across all channels, while a relatively large change occurred at the second addition. The logarithm of final salt concentration has previously been shown to be proportional to conductance change in the linear on-regime [52]. Figure 2.11e shows the signal change presented in terms of this logarithmic relationship. The median values of the first two additions do not line up well with the overall logarithmic trend; insufficient mixing in the tightly enclosed PDMS well environment for the first few additions may be responsible for this result. Subsequent additions may improve mixing in the well, leading to the change in concentration at the surface of the channel being more representative of the overall concentration in the well.

In Figure 2.11b and Figure 2.11c, from around the second deionised water addition onwards, the drift behaviours of individual channels begin to significantly diverge. This deviation from the baseline drift subtracted from the raw data occurs either because the linear fit is only a first-order approximation which weakens with time, or because the additions themselves affect the drift behaviour. Displaying the data as discrete signal changes, as in Figure 2.11d, is one way of excluding these deviations (see Section B.4). An alternative way of presenting the signal changes, by normalising relative to both I_0 and the final current reading with the formula $(I - I_0)/(I_f - I_0)$, is shown in Figure 2.12. This

2.4. Aqueous Sensing of Phosphate Buffered Saline Concentration

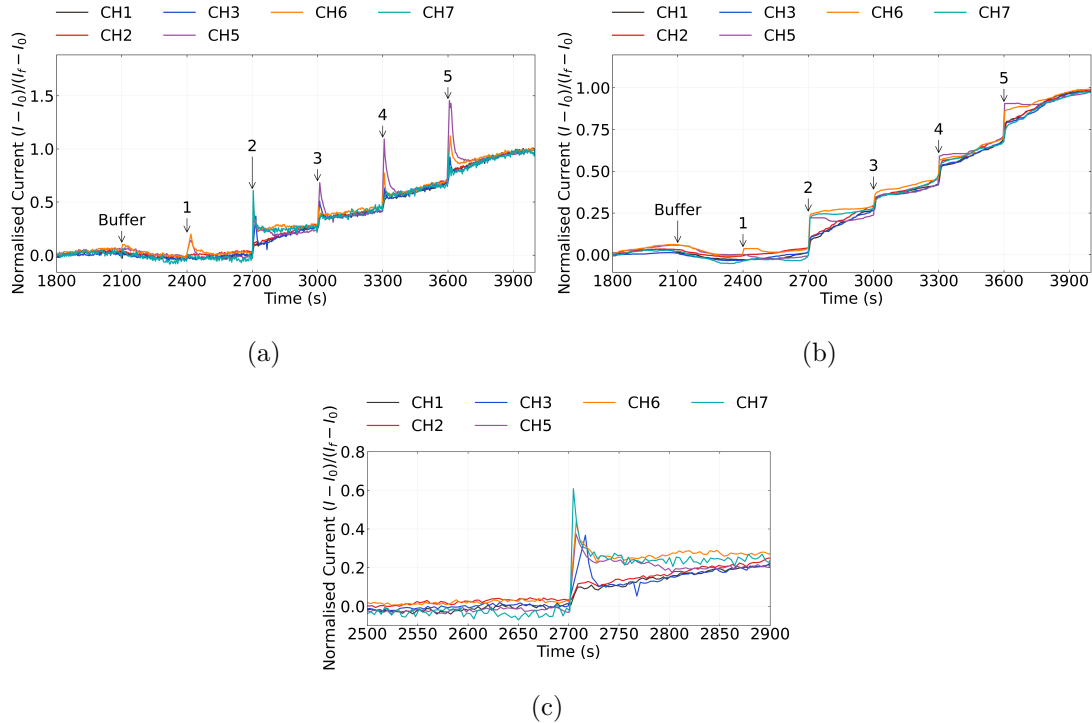


Figure 2.12.: The processed data shown in Figure 2.11b and Figure 2.11c is normalised to I_0 , but an alternative normalisation can more effectively filter out remaining drift present. This normalisation presents data relative to both I_0 and the final current reading I_f using the formula $(I - I_0)/(I_f - I_0)$. Using this normalisation, the data in Figure 2.11b and Figure 2.11c can be displayed instead as (a) and (b) respectively. (c) shows a magnified version of the step at addition 2 in (a).

2. Characteristics of Pristine Carbon Nanotube & Graphene Field Effect Transistors

approach is useful for filtering out remaining unaccounted-for drift behaviour in order to compare the short-term transient responses to additions across the device channels. Furthermore, it lets us better understand how the short-term transient responses affect the longer-term step responses discussed earlier.

Figure 2.12a and Figure 2.12c show that the transient responses to DI water additions vary significantly across the surface of the device. For example, Figure 2.12c shows that in response to the second DI water addition, channel 7 gives a large initial transient response about twice the size of the step increase between 2600 and 2800 s. Meanwhile, channels 1 and 2 show no transient response above the step increase. Figure 2.12c indicates transient size is based on location across the device, with neighbouring channels showing the most similar behaviour. This spatially-dependent behaviour may indicate transient responses are determined by the location of the channel relative to either the location of water additions or the slightly-variable location of the liquid gate. Larger and longer-lasting transient responses are not entirely removed by the moving median filter, as shown by comparing Figure 2.12a to Figure 2.11c, and so careful placement of additions is important when sensing to minimise this effect. However, even the longest-lasting transients appear to decay to zero within about 200 s, demonstrating that a 200 s spacing between additions at minimum is necessary for reliable real-time liquid-gated sensing using this setup.

Signal-to-Noise Ratio

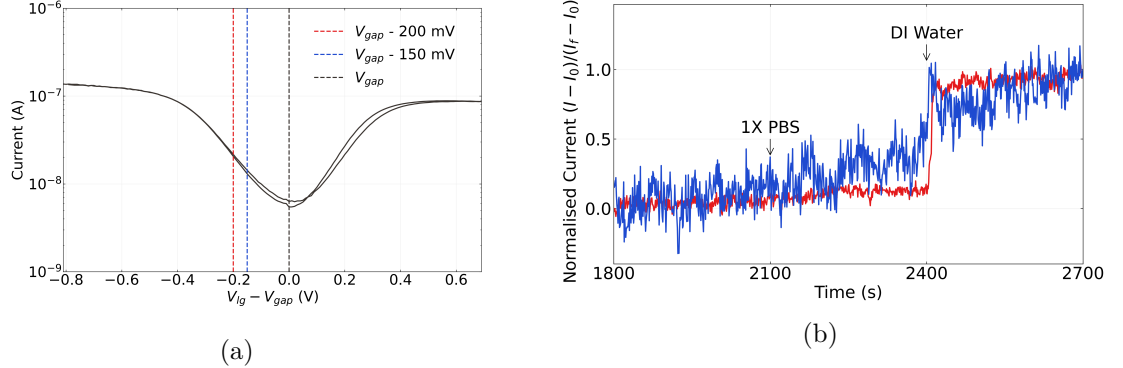


Figure 2.13.: The transfer characteristics of a single steam-deposited carbon nanotube field-effect transistor channel are shown in (a). V_{gap} is the gate voltage corresponding to the center of the transistor bandgap, found at the minimum of the characteristic curve. The signal-to-noise ratio of the channel response to a deionised water addition after a suitable control series is shown in (b). The blue current trace in (b) was performed gating the device 150 mV away from V_{gap} , while the red current was performed gating the device 200 mV away from V_{gap} .

To understand the effect of gate voltages on signal-to-noise ratio, two PBS control and salt concentration sensing series were performed with the same channel at different gate voltages. The transfer characteristics of this channel are shown in Figure 2.13a, with coloured dashed lines marking the voltages used for gating the transistor during each sensing series. Figure 2.13 shows the initial PBS and DI water additions made after 1800 s. Previous work on the signal-to-noise ratio for liquid-gated, encapsulated carbon nanotube devices suggests that gating devices close to V_{gap} should give the largest signal-to-noise ratio for salt concentration additions [33]. However, this was not what was observed for our carbon nanotube field-effect transistor, as Figure 2.13 shows improved signal-to-noise ratio, i.e. the signal step can be more clearly distinguished, when gated at a voltage further removed from V_{gap} . This discrepancy could be a result of the use of a network of carbon nanotubes rather than a single nanotube; gating may have less of an impact on noise when a network morphology is used. Alternatively, it could be a result of a lack of mixing in our static well setup leading to inconsistent signal sizes with concentration change. Heller *et al.* used a flow cell during their signal-to-ratio work [33]. By using a flow cell with our devices, it would be possible to confirm whether this is the case, and this might also help us reduce the size of unwanted transient responses resulting from drop-wise additions.

2.5. Vapour Sensing with Ethyl Hexanoate

2.5.1. Baseline Drift

When sensing vapour in the vapour delivery system, devices have no liquid gate and are instead backgated when taking measurements. Therefore, the baseline drift of devices characterised in this manner should be considered separately to those characterised in an liquid-gated environment. Device baseline drift of a backgated device in the vapour sensing chamber is therefore examined here in more detail.

The magnitude of baseline drift is lower for our devices than for those characterised by Noyce *et al.*, which may be a result of numerous device and setup differences which affect the presence of charge traps. These differences include liquid-gating instead of back-gated, the use of a network of carbon nanotubes instead of single nanotubes, a different channel length, the use of a 300 nm instead of 90 nm SiO₂ layer, and the use of an asymmetric, liquid-gated transfer sweep over a shorter voltage range to characterise devices before each control series was measured [61].

2. Characteristics of Pristine Carbon Nanotube & Graphene Field Effect Transistors

2.5.2. Sensing Series

2.6. Conclusion

To ensure fabricated transistors were suitable for biosensing purposes, the morphology and electrical properties of the pristine carbon nanotube and graphene transistors were investigated.

The morphology of the carbon nanotube networks were found to have a significant impact on the electrical characteristics of the devices, which was determined through comparison of the skew-normal height profile of the carbon nanotube network and the key electrical parameters of a range of carbon nanotube devices. When networks were highly bundled ($> 90\%$), there was a large range of carbon nanotube bundle diameters present in the network. This large variation in the size of conducting pathways resulted in a wide range of on-off ratios and threshold voltages for the liquid-gated devices created using these carbon nanotube films. In contrast, devices using films fabricated with a relatively low percentage of bundling ($< 75\%$) showed highly consistent on-off ratios and threshold voltages, along with low hysteresis, due to the relatively consistent bundle diameters and high density of these networks. These low-bundling networks were found to have a mean bundle distribution height of 3.3 ± 1.0 nm. When performing multiplexed sensing, consistent channel behaviour is highly desirable since comparing sensing behaviour between channels is more straightforward.

However, atomic force microscope imaging and Raman spectroscopy also indicated that less bundled networks had the most surface contamination present. Aggregated surfactant present on the surface had a height of more than 4 nm, and introduced significant defects to the carbon nanotube network. The introduction of *p*-dopants to the carbon nanotubes by surfactant appears to have significantly increased the threshold voltage of steam-assisted surfactant-deposited network devices relative to steam-free surfactant-deposited network devices. Since the presence of surfactant could negatively impact biosensing, techniques to remove contaminants should be explored in more detail. Oxidation and thermal annealing of carbon nanotube films at high temperatures could be used to resolve this issue, and this is discussed further in [?@sec-future-work](#). The presence of electrolyte on the surface of a backgated transistor for use in vapour sensing was also found to significantly adversely affect its electrical characteristics.

Constant voltage real-time measurements of the carbon nanotube field-effect transistor devices had a characteristic drift that could be modelled using a exponential and linear term. The linear term of baseline drift had a reasonably consistent gradient between device channels, with a mean value of -6.1 ± 1.2 , indicating that similar drift behaviour should be reproducible between devices fabricated in the same manner. The time constant of the exponential term ranged from $\tau = 330 \pm 20$ s to $\tau = 800 \pm 750$ for the device characterised. These results indicate that the PBS control series is asuitable time length

2.6. Conclusion

for minimising the effects of baseline drift on sensing, since the range of time constants are all well below the total timescale of the control series.

Salt concentration or PBS dilution sensing series indicated that the carbon nanotube transistor devices were highly sensitive to environmental changes and therefore suitable for sensing work. Successive additions of deionised water to the 1XPBS present in the well gave signal responses of up to 2.5 % above the control response. The signal response was found to be proportional to the logarithm of concentration, giving a fit to the median response sizes with an $R^2 = 0.86$. Deviations from this trend can possibly be explained by the enclosed sensing environment preventing sufficient mixing of electrolyte concentrations within the PDMS well, which could possibly be addressed by using a flow cell for sensing work. It was also seen that the signal size relative to baseline drift was highly consistent between channels. This is a promising result when it comes to ensuring consistent multiplexing, but it cannot be guaranteed that this behaviour carries over to sensing with biofunctionalised devices.

Graphene field-effect transistor devices were often found to possess a double-minima feature, which appears to be the result of a lack of doping from the metal contacts in the center of the device channels. These double Dirac points are unlikely to have an significant effect on the sensing behaviour of graphene devices. The graphene device characteristics were found to be consistent after 1 hour exposure to 1X PBS with minimal drift, with an on-off ratio of 5 and major Dirac point voltage of 0.3 V. There was some indications from the transfer characteristics that *p*-dopants were present on the graphene surface. Salt concentration sensing with graphene FETs is not shown in this thesis, but it is important to perform this experiment and use similar analysis techniques if there are any concerns about the sensitivity of a fabricated batch of graphene devices.

A. Vapour System Hardware

Table A.1.: Major components used in construction of the vapour delivery system described in this thesis.

Description	Part No.	Manufacturer
Mass flow controller, 20 sccm full scale	GE50A013201SBV020	MKS Instruments
Mass flow controller, 200 sccm full scale	GE50A013202SBV020	MKS Instruments
Mass flow controller, 500 sccm full scale	FC-2901V	Tylan
Analogue flowmeter, 240 sccm max. flow	116261-30	Dwyer
Micro diaphragm pump	P200-B3C5V-35000	Xavitech
Analogue flow controller, for micro diaphragm pump	X3000450	Xavitech
10 mL Schott bottle	218010802	Duran
PTFE connection cap system	Z742273	Duran
Baseline VOC-TRAQ flow cell, red	043-951	Mocon
Humidity and temperature sensor	T9602	Telaire
Enclosure, for humidity and temperature sensor	MC001189	Multicomp Pro

B. Python Code for Data Analysis

B.1. Code Repository

The code used for general analysis of field-effect transistor devices in this thesis was written with Python 3.8.8. Contributors to the code used include Erica Cassie, Erica Happe, Marissa Dierkes and Leo Browning. The code is located on GitHub and the research group OneDrive, and is available on request.

B.2. Atomic Force Microscope Histogram Analysis

The purpose of this code is to analyse atomic force microscope (AFM) images of carbon nanotube networks in .xyz format taken using an atomic force microscope and processed in Gwyddion (see [?@sec-afm-characterisation](#)). It was originally designed by Erica Happe in Matlab, and adapted by Marissa Dierkes and myself for use in Python. The code imports the .xyz data and sorts it into bins 0.15 nm in size for processing. To perform skew-normal distribution fits, both *scipy.optimize.curve_fit* and *scipy.stats.skewnorm* modules are used in this code.

B.3. Raman Spectroscopy Analysis

The purpose of this code is to analyse a series of Raman spectra taken at different points on a single film (see [?@sec-raman-characterisation](#)). Data is imported in a series of tab-delimited text files, with the low wavenumber spectrum ($100\text{ cm}^{-1} - 650\text{ cm}^{-1}$) and high wavenumber spectrum ($1300\text{ cm}^{-1} - 1650\text{ cm}^{-1}$) imported in separate datafiles for each scan location.

B.4. Field-Effect Transistor Analysis

The purpose of this code is to analyse electrical measurements taken of field-effect transistor (FET) devices. Electrical measurements were either taken from the Keysight 4156C Semiconductor Parameter Analyser, National Instruments NI-PXIe or Keysight B1500A Semiconductor Device Analyser as discussed in [?@sec-electrical-characterisation](#);

B. Python Code for Data Analysis

the code is able to analyse data in .csv format taken from all three measurement setups. The main Python file in the code base consists of three related but independent modules: the first analyses and plots sensing data from the FET devices, the second analyses and plots transfer characteristics from channels across a device, and the third compares individual channel characteristics before and after a modification or after each of several modifications. The code base also features a separate config file and style sheet which govern the behaviour of the main code. The code base was designed collaboratively by myself and Erica Cassie over GitHub using the Sourcetree Git GUI.

Bibliography

- [1] “piD-TECH® eVx User Manual 143-175 Rev 1.0”. URL: <https://www.ametekmocon.com/products/oemphotoionization/pidtechevxphotoionizationdetector>.
- [2] *Technical Application Articles - Ion Science UK*. URL: <https://ionscience.com/en/gas-and-leak-detectors/customer-support/support-documents/technical-application-articles/> (visited on 2024-02-27).
- [3] Amphenol Advanced Sensors. *Telaire T9602 Humidity and Temperature Sensor*. (Visited on 2024-02-26).
- [4] *The Capacitive Humidity Sensor*. URL: https://www.rotronic.com/en/humidity-measurement-feuchtemessung-mesure_de_1_humidite/capacitive-sensors-technical-notes-mr (visited on 2024-02-26).
- [5] *Make Your Job Easier with Humidity Conversion Formulas / Vaisala*. URL: <https://www.vaisala.com/en/lp/make-your-job-easier-humidity-conversion-formulas> (visited on 2024-02-26).
- [6] H. Y. Zheng and N. O.V. Plank. “Facile fabrication of carbon nanotube network thin film transistors for device platforms”. In: *International Journal of Nanotechnology* 14.1-6 (2017), pp. 505–518. ISSN: 14757435. DOI: 10.1504/IJNT.2017.082473.
- [7] Thanihaichelvan Murugathas, Leo A. Browning, Marissa P. Dierkes, et al. “Data on liquid gated CNT network FETs on flexible substrates”. In: *Data in Brief* 21 (Dec. 2018), pp. 276–283. ISSN: 2352-3409. DOI: 10.1016/J.DIB.2018.09.093.
- [8] Thanihaichelvan Murugathas, Leo A. Browning, Marissa P. Dierkes, et al. “Metallic-semiconducting junctions create sensing hot-spots in carbon nanotube FET aptasensors near percolation”. In: *Biosensors and Bioelectronics* 130 (Apr. 2019), pp. 408–413. ISSN: 0956-5663. DOI: 10.1016/J.BIOS.2018.09.021.
- [9] Hong Phan T. Nguyen, Thanihaichelvan Murugathas, and Natalie O.V. Plank. “Comparison of Duplex and Quadruplex Folding Structure Adenosine Aptamers for Carbon Nanotube Field Effect Transistor Aptasensors”. In: *Nanomaterials (Basel, Switzerland)* 11.9 (Sept. 2021). ISSN: 2079-4991. DOI: 10.3390/NANO11092280. URL: <https://pubmed.ncbi.nlm.nih.gov/34578596/>.

Bibliography

- [10] Wim Wenseleers, Igor L. Vlasov, Etienne Goovaerts, et al. “Efficient Isolation and Solubilization of Pristine Single-Walled Nanotubes in Bile Salt Micelles”. In: *Advanced Functional Materials* 14.11 (Nov. 2004), pp. 1105–1112. ISSN: 1616-3028. DOI: 10.1002/ADFM.200400130. URL: <https://onlinelibrary.wiley.com/doi/full/10.1002/adfm.200400130%20https://onlinelibrary.wiley.com/doi/abs/10.1002/adfm.200400130%20https://onlinelibrary.wiley.com/doi/10.1002/adfm.200400130>.
- [11] Gildas Gavrel, Bruno Jousselme, Arianna Filoromo, et al. “Supramolecular Chemistry of Carbon Nanotubes”. In: (2013), pp. 95–126. DOI: 10.1007/128_2013_450.
- [12] Greg T. Hermanson. “Buckyballs, Fullerenes, and Carbon Nanotubes”. In: *Bioconjugate Techniques* (Jan. 2013), pp. 741–755. DOI: 10.1016/B978-0-12-382239-0.00016-9.
- [13] Maki Shimizu, Shunjiro Fujii, Takeshi Tanaka, et al. “Effects of surfactants on the electronic transport properties of thin-film transistors of single-wall carbon nanotubes”. In: *Journal of Physical Chemistry C* 117.22 (June 2013), pp. 11744–11749. ISSN: 19327455. DOI: 10.1021/JP3113254/SUPPL_FILE/JP3113254_SI_001.PDF. URL: <https://pubs.acs.org/doi/full/10.1021/jp3113254>.
- [14] Antonello Di Crescenzo, Valeria Ettorre, and Antonella Fontana. “Non-covalent and reversible functionalization of carbon nanotubes”. In: *Beilstein Journal of Nanotechnology* 5.1 (2014), p. 1675. ISSN: 21904286. DOI: 10.3762/BJNANO.5.178. URL: /pmc/articles/PMC4222398/%20/pmc/articles/PMC4222398/?report=abstract%20https://www.ncbi.nlm.nih.gov/pmc/articles/PMC4222398/.
- [15] Melburne C. LeMieux, Mark Roberts, Soumendra Barman, et al. “Self-sorted, aligned nanotube networks for thin-film transistors”. In: *Science* 321.5885 (July 2008), pp. 101–104. ISSN: 00368075. DOI: 10.1126/SCIENCE.1156588. URL: <https://www.science.org>.
- [16] Chang Liu and Hui Ming Cheng. “Carbon nanotubes: controlled growth and application”. In: *Materials Today* 16.1-2 (Jan. 2013), pp. 19–28. ISSN: 1369-7021. DOI: 10.1016/J.MATTOD.2013.01.019.
- [17] Dusan Vobornik, Maohui Chen, Shan Zou, et al. “Measuring the Diameter of Single-Wall Carbon Nanotubes Using AFM”. In: *Nanomaterials* 13.3 (Feb. 2023), p. 477. ISSN: 20794991. DOI: 10.3390/NANO13030477/S1. URL: <https://www.mdpi.com/2079-4991/13/3/477/htm%20https://www.mdpi.com/2079-4991/13/3/477>.
- [18] A. Azzalini and A. Capitanio. “Statistical applications of the multivariate skew normal distribution”. In: *Journal of the Royal Statistical Society Series B* 61.3 (1999), pp. 579–602. ISSN: 13697412. DOI: 10.1111/1467-9868.00194. arXiv: 0911.2093. URL: <https://ideas.repec.org/a/bla/jorssb/v61y1999i3p579-602.html>.

- [19] Matěj Velický, Adam J Cooper, Peter S Toth, et al. “Mechanical stability of substrate-bound graphene in contact with aqueous solutions”. In: *2D Materials* 2.2 (May 2015), p. 024011. ISSN: 2053-1583. DOI: 10.1088/2053-1583/2/2/024011. URL: <https://iopscience.iop.org/article/10.1088/2053-1583/2/2/024011%20https://iopscience.iop.org/article/10.1088/2053-1583/2/2/024011/meta>.
- [20] Erin E. Christensen, Mitesh Amin, Trevor M. Tumiel, et al. “Localized Charge on Surfactant-Wrapped Single-Walled Carbon Nanotubes”. In: *Journal of Physical Chemistry Letters* 13.46 (Nov. 2022), pp. 10705–10712. ISSN: 19487185. DOI: 10.1021/ACS.JPCLETT.2C02650. URL: <https://pubs.acs.org/doi/full/10.1021/acs.jpclett.2c02650>.
- [21] R. L. Graham, B. D. Lubachevsky, K. J. Nurmela, et al. “Dense packings of congruent circles in a circle”. In: *Discrete Mathematics* 181.1-3 (Feb. 1998), pp. 139–154. ISSN: 0012-365X. DOI: 10.1016/S0012-365X(97)00050-2.
- [22] Eckard Specht. *The best known packings of equal circles in a circle*. URL: <http://hydra.nat.uni-magdeburg.de/packing/cci/cci.html> (visited on 2023-09-11).
- [23] Robert D. Deegan, Olgica Bakajin, Todd F. Dupont, et al. “Capillary flow as the cause of ring stains from dried liquid drops”. In: *Nature* 1997 389:6653 389.6653 (1997), pp. 827–829. ISSN: 1476-4687. DOI: 10.1038/39827. URL: <https://www.nature.com/articles/39827>.
- [24] R. T. van Gaalen, C. Diddens, H. M.A. Wijshoff, et al. “Marangoni circulation in evaporating droplets in the presence of soluble surfactants”. In: *Journal of Colloid and Interface Science* 584 (Feb. 2021), pp. 622–633. ISSN: 0021-9797. DOI: 10.1016/J.JCIS.2020.10.057.
- [25] Mindy D. Bishop, Gage Hills, Tathagata Srimani, et al. “Fabrication of carbon nanotube field-effect transistors in commercial silicon manufacturing facilities”. In: *Nature Electronics* 2020 3:8 3.8 (June 2020), pp. 492–501. ISSN: 2520-1131. DOI: 10.1038/s41928-020-0419-7. URL: <https://www.nature.com/articles/s41928-020-0419-7>.
- [26] Yulia V Marchenko and Marc G Genton. “A suite of commands for fitting the skew-normal and skew-t models”. In: *The Stata Journal* 10.4 (2010), pp. 507–539.
- [27] Alexander A. Kane, Alexandra C. Ford, April Nissen, et al. “Etching of surfactant from solution-processed, type-separated carbon nanotubes and impact on device behavior”. In: *ACS Nano* 8.3 (Mar. 2014), pp. 2477–2485. ISSN: 1936086X. DOI: 10.1021/NN406065T. URL: <https://pubs.acs.org/doi/full/10.1021/nn406065t>.
- [28] Millie S. Dresselhaus, G. Dresselhaus, R. Saito, et al. “Raman spectroscopy of carbon nanotubes”. In: *Physics Reports* 409.2 (Mar. 2005), pp. 47–99. ISSN: 0370-1573. DOI: 10.1016/J.PHYSREP.2004.10.006.

Bibliography

- [29] Benjamin King and Balaji Panchapakesan. “Vacuum filtration based formation of liquid crystal films of semiconducting carbon nanotubes and high performance transistor devices”. In: *Nanotechnology* 25.17 (Apr. 2014), p. 175201. ISSN: 0957-4484. DOI: 10.1088/0957-4484/25/17/175201. URL: <https://iopscience.iop.org/article/10.1088/0957-4484/25/17/175201%20https://iopscience.iop.org/article/10.1088/0957-4484/25/17/175201/meta>.
- [30] M. Świniarski, A. Dużyńska, A. P. Gertych, et al. “Determination of the electronic transport in type separated carbon nanotubes thin films doped with gold nanocrystals”. In: *Scientific Reports* 2021 11:1 11.1 (Aug. 2021), pp. 1–7. ISSN: 2045-2322. DOI: 10.1038/s41598-021-96307-6. URL: <https://www.nature.com/articles/s41598-021-96307-6>.
- [31] David C. Stone. “Application of median filtering to noisy data”. In: 73.10 (Oct. 2011), pp. 1573–1581. ISSN: 0008-4042. DOI: 10.1139/V95-195. URL: <https://cdnsciencepub.com/doi/10.1139/v95-195>.
- [32] Douglas R. Kauffman and Alexander Star. “Electronically monitoring biological interactions with carbon nanotube field-effect transistors”. In: *Chemical Society Reviews* 37.6 (May 2008), pp. 1197–1206. ISSN: 1460-4744. DOI: 10.1039/B709567H. URL: <https://pubs.rsc.org/en/content/articlehtml/2008/cs/b709567h%20https://pubs.rsc.org/en/content/articlelanding/2008/cs/b709567h>.
- [33] Iddo Heller, Jaan Mānnik, Serge G. Lemay, et al. “Optimizing the signal-to-noise ratio for biosensing with carbon nanotube transistors”. In: *Nano Letters* 9.1 (Jan. 2009), pp. 377–382. ISSN: 15306984. DOI: 10.1021/NL8031636/SUPPL_FILE/NL8031636_SI_001.PDF. URL: <https://pubs.acs.org/doi/full/10.1021/nl8031636>.
- [34] Woo Jong Yu, Un Jeong Kim, Bo Ram Kang, et al. “Adaptive Logic Circuits with Doping-Free Ambipolar Carbon Nanotube Transistors”. In: *NANO LETTERS* 9.4 (2009), pp. 1401–1405. DOI: 10.1021/nl803066v. URL: <https://pubs.acs.org/sharingguidelines>.
- [35] Vladimir Derenskyi, Widiantha Gomulya, Jorge Mario Salazar Rios, et al. “Carbon Nanotube Network Ambipolar Field-Effect Transistors with 108 On/Off Ratio”. In: *Advanced Materials* 26.34 (Sept. 2014), pp. 5969–5975. ISSN: 15214095. DOI: 10.1002/ADMA.201401395.
- [36] Faris M. Albarghouthi, Nicholas X. Williams, James L. Doherty, et al. “Passivation Strategies for Enhancing Solution-Gated Carbon Nanotube Field-Effect Transistor Biosensing Performance and Stability in Ionic Solutions”. In: *ACS Applied Nano Materials* 5.10 (Oct. 2022), pp. 15865–15874. ISSN: 25740970. DOI: 10.1021/ACSANM.2C04098/SUPPL_FILE/AN2C04098_SI_001.PDF. URL: <https://doi.org/10.1021/acsanm.2c04098>.

- [37] Eric Pop, Sumit Dutta, David Estrada, et al. “Avalanche, Joule breakdown and hysteresis in carbon nanotube transistors”. In: *IEEE International Reliability Physics Symposium Proceedings* (2009), pp. 405–408. ISSN: 15417026. DOI: 10.1109/IRPS.2009.5173287.
- [38] Nima Rouhi, Dheeraj Jain, Katayoun Zand, et al. “Fundamental limits on the mobility of nanotube-based semiconducting inks”. In: *Advanced Materials* 23.1 (Jan. 2011), pp. 94–99. ISSN: 09359648. DOI: 10.1002/ADMA.201003281.
- [39] Jana Zaumseil. “Single-walled carbon nanotube networks for flexible and printed electronics”. In: *Semiconductor Science and Technology* 30.7 (June 2015), p. 074001. ISSN: 0268-1242. DOI: 10.1088/0268-1242/30/7/074001. URL: <https://iopscience.iop.org/article/10.1088/0268-1242/30/7/074001%20https://iopscience.iop.org/article/10.1088/0268-1242/30/7/074001/meta>.
- [40] Xuan P A Gao, Gengfeng Zheng, and Charles M Lieber. “Subthreshold Regime has the Optimal Sensitivity for Nanowire FET Biosensors”. In: (2010). DOI: 10.1021/nl9034219. URL: <https://pubs.acs.org/sharingguidelines>.
- [41] Donghun Kang, Noejung Park, Ju Hye Ko, et al. “Oxygen-induced p-type doping of a long individual single-walled carbon nanotube”. In: *Nanotechnology* 16.8 (May 2005), p. 1048. ISSN: 0957-4484. DOI: 10.1088/0957-4484/16/8/008. URL: <https://iopscience.iop.org/article/10.1088/0957-4484/16/8/008%20https://iopscience.iop.org/article/10.1088/0957-4484/16/8/008/meta>.
- [42] Iddo Heller, Anne M. Janssens, Jaan Männik, et al. “Identifying the mechanism of biosensing with carbon nanotube transistors”. In: *Nano Letters* 8.2 (Feb. 2008), pp. 591–595. ISSN: 15306984. DOI: 10.1021/NL072996I. URL: <https://pubs.acs.org/doi/full/10.1021/nl072996i>.
- [43] Yoshiyuki Nonoguchi, Atsushi Tani, Tomoko Murayama, et al. “Surfactant-driven Amphoteric Doping of Carbon Nanotubes”. In: *Chemistry - An Asian Journal* 13.24 (Dec. 2018), pp. 3942–3946. ISSN: 1861471X. DOI: 10.1002/ASIA.201801490.
- [44] Chris J. Barnett, Cathren E. Gowenlock, Kathryn Welsby, et al. “Spatial and Contamination-Dependent Electrical Properties of Carbon Nanotubes”. In: *Nano letters* 18.2 (Feb. 2018), pp. 695–700. ISSN: 1530-6992. DOI: 10.1021/ACS.NANOLETT.7B03390. URL: <https://pubmed.ncbi.nlm.nih.gov/29257695/>.
- [45] Joon Sung Lee, Sunmin Ryu, Kwonjae Yoo, et al. “Origin of gate hysteresis in carbon nanotube field-effect transistors”. In: *Journal of Physical Chemistry C* 111.34 (Aug. 2007), pp. 12504–12507. ISSN: 19327447. DOI: 10.1021/JP074692Q/ASSET/IMAGES/LARGE/JP074692QF00003.JPG. URL: <https://pubs.acs.org/doi/full/10.1021/jp074692q>.
- [46] Sang Won Lee, Si Young Lee, Seong Chu Lim, et al. “Positive gate bias stress instability of carbon nanotube thin film transistors”. In: *Applied Physics Letters* 101.5 (July 2012). ISSN: 00036951. DOI: 10.1063/1.4740084/111432. URL: [/aip/apl/article/101/5/053504/111432/Positive-gate-bias-stress-instability-of-carbon](https://aip.org/article/101/5/053504/111432/Positive-gate-bias-stress-instability-of-carbon).

Bibliography

- [47] Tae Jun Ha, Daisuke Kiriya, Kevin Chen, et al. “Highly stable hysteresis-free carbon nanotube thin-film transistors by fluorocarbon polymer encapsulation”. In: *ACS Applied Materials and Interfaces* 6.11 (June 2014), pp. 8441–8446. ISSN: 19448252. DOI: 10.1021/AM5013326/ASSET/IMAGES/LARGE/AM-2014-013326_0007.JPG. URL: <https://pubs.acs.org/doi/full/10.1021/am5013326>.
- [48] Woong Kim, Ali Javey, Ophir Vermesh, et al. “Hysteresis Caused by Water Molecules in Carbon Nanotube Field-Effect Transistors”. In: *NANO LETTERS* 3.2 (2003), pp. 193–198. DOI: 10.1021/nl0259232.
- [49] Aaron D. Franklin, George S. Tulevski, Shu Jen Han, et al. “Variability in carbon nanotube transistors: Improving device-to-device consistency”. In: *ACS Nano* 6.2 (Feb. 2012), pp. 1109–1115. ISSN: 19360851. DOI: 10.1021/NN203516Z/SUPPLFILE/NN203516Z_SI_001.PDF. URL: <https://pubs.acs.org/doi/full/10.1021/nn203516z>.
- [50] Helene Conseil, Morten S. Jellesen, and Rajan Ambat. “Experimental study of water absorption of electronic components and internal local temperature and humidity into electronic enclosure”. In: *Proceedings of the 16th Electronics Packaging Technology Conference, EPTC 2014* (Jan. 2014), pp. 355–359. DOI: 10.1109/EPTC.2014.7028356.
- [51] I. Heller, S. Chattoor, J. Männik, et al. “Comparing the weak and strong gate-coupling regimes for nanotube and graphene transistors”. In: *physica status solidi (RRL) – Rapid Research Letters* 3.6 (Sept. 2009), pp. 190–192. ISSN: 1862-6270. DOI: 10.1002/PSSR.200903157. URL: <https://onlinelibrary.wiley.com/doi/full/10.1002/pssr.200903157%20https://onlinelibrary.wiley.com/doi/abs/10.1002/pssr.200903157%20https://onlinelibrary.wiley.com/doi/10.1002/pssr.200903157>.
- [52] Iddo Heller, Sohail Chattoor, Jaan Männik, et al. “Influence of electrolyte composition on liquid-gated carbon nanotube and graphene transistors”. In: *Journal of the American Chemical Society* 132.48 (Dec. 2010), pp. 17149–17156. ISSN: 00027863. DOI: 10.1021/JA104850N/SUPPLFILE/JA104850N_SI_001.PDF. URL: <https://pubs.acs.org/doi/full/10.1021/ja104850n>.
- [53] Fengnian Xia, Damon B. Farmer, Yu Ming Lin, et al. “Graphene field-effect transistors with high on/off current ratio and large transport band gap at room temperature”. In: *Nano Letters* 10.2 (Feb. 2010), pp. 715–718. ISSN: 15306984. DOI: 10.1021/NL9039636/ASSET/IMAGES/LARGE/NL-2009-039636_0003.JPG. URL: <https://pubs.acs.org/doi/full/10.1021/nl9039636>.
- [54] Dmitry Kireev, Max Brambach, Silke Seyock, et al. “Graphene transistors for interfacing with cells: towards a deeper understanding of liquid gating and sensitivity”. In: *Scientific Reports* 2017 7:1 7.1 (July 2017), pp. 1–12. ISSN: 2045-2322. DOI: 10.1038/s41598-017-06906-5. URL: <https://www.nature.com/articles/s41598-017-06906-5>.

- [55] Antonio Di Bartolomeo, Filippo Giubileo, Salvatore Santandrea, et al. “Charge transfer and partial pinning at the contacts as the origin of a double dip in the transfer characteristics of graphene-based field-effect transistors”. In: *Nanotechnology* 22.27 (May 2011), p. 275702. ISSN: 0957-4484. DOI: 10.1088/0957-4484/22/27/275702. URL: <https://iopscience.iop.org/article/10.1088/0957-4484/22/27/275702%20https://iopscience.iop.org/article/10.1088/0957-4484/22/27/275702/meta>.
- [56] Zengguang Cheng, Qiaoyu Zhou, Chenxuan Wang, et al. “Toward intrinsic graphene surfaces: A systematic study on thermal annealing and wet-chemical treatment of SiO₂-supported graphene devices”. In: *Nano Letters* 11.2 (Feb. 2011), pp. 767–771. ISSN: 15306984. DOI: 10.1021/NL103977D/SUPPL_FILE/NL103977D_SI_001.PDF. URL: <https://pubs.acs.org/doi/full/10.1021/nl103977d>.
- [57] Dong Wook Shin, Hyun Myoung Lee, Seong Man Yu, et al. “A facile route to recover intrinsic graphene over large scale”. In: *ACS Nano* 6.9 (Sept. 2012), pp. 7781–7788. ISSN: 19360851. DOI: 10.1021/NN3017603/SUPPL_FILE/NN3017603_SI_001.PDF. URL: <https://pubs.acs.org/doi/full/10.1021/mn3017603>.
- [58] Tingting Feng, Dan Xie, Jianlong Xu, et al. “Back-gate graphene field-effect transistors with double conductance minima”. In: *Carbon* 79.1 (Nov. 2014), pp. 363–368. ISSN: 0008-6223. DOI: 10.1016/J.CARBON.2014.07.078.
- [59] Song ang Peng, Zhi Jin, Dayong Zhang, et al. “How Do Contact and Channel Contribute to the Dirac Points in Graphene Field-Effect Transistors?” In: *Advanced Electronic Materials* 4.8 (Aug. 2018), p. 1800158. ISSN: 2199-160X. DOI: 10.1002/AELM.201800158. URL: <https://onlinelibrary.wiley.com/doi/full/10.1002/aelm.201800158%20https://onlinelibrary.wiley.com/doi/abs/10.1002/aelm.201800158%20https://onlinelibrary.wiley.com/doi/10.1002/aelm.201800158>.
- [60] Y. Bargaoui, M. Troudi, P. Bondavalli, et al. “Gate bias stress effect in single-walled carbon nanotubes field-effect-transistors”. In: *Diamond and Related Materials* 84 (Apr. 2018), pp. 62–65. ISSN: 0925-9635. DOI: 10.1016/J.DIAMOND.2018.03.011.
- [61] Steven G. Noyce, James L. Doherty, Zhihui Cheng, et al. “Electronic Stability of Carbon Nanotube Transistors under Long-Term Bias Stress”. In: *Nano Letters* 19.3 (Mar. 2019), pp. 1460–1466. ISSN: 15306992. DOI: 10.1021/ACS.NANOLETT.8B03986/ASSET/IMAGES/LARGE/NL-2018-03986G_0005.JPG. URL: <https://pubs.acs.org/doi/full/10.1021/acs.nanolett.8b03986>.
- [62] H. Lin and S. Tiwari. “Localized charge trapping due to adsorption in nanotube field-effect transistor and its field-mediated transport”. In: *Applied Physics Letters* 89.7 (Aug. 2006), p. 73507. ISSN: 00036951. DOI: 10.1063/1.2337104. URL: [/aip/apl/article/89/7/073507/332595/Localized-charge-trapping-due-to-adsorption-in](https://aip.org/apl/article/89/7/073507/332595/Localized-charge-trapping-due-to-adsorption-in).